UC Riverside
UC Riverside Previously Published Works

Title

The Impact of Extended H2O Cross Sections on Temperate Anoxic Planet Atmospheres: Implications for Spectral Characterization of Habitable Worlds

Permalink

https://escholarship.org/uc/item/66z3v6mp

Journal

The Astrophysical Journal, 967(2)

ISSN

0004-637X

Authors

Broussard, Wynter

Schwieterman, Edward W

Ranjan, Sukrit

et al.

Publication Date

2024-06-01

DOI

10.3847/1538-4357/ad3a65

Copyright Information

Peer reviewed

The Impact of Extended H₂O Cross Sections on Temperate Anoxic Planet Atmospheres: Implications for Spectral Characterization of Habitable Worlds

Wynter Broussard[1] , Edward W. Schwieterman[1,2] , Sukrit Ranjan[2,3] , Clara Sousa-Silva[4,5] , Alexander Fateev[6] , and Christopher T. Reinhard[7]

[1] Department of Earth and Planetary Sciences, University of California, Riverside, CA 92521, USA; abrou009@ucr.edu
[2] Blue Marble Space Institute of Science, Seattle, WA 98154, USA
[3] University of Arizona, Lunar and Planetary Laboratory/Department of Planetary Sciences, Tucson, AZ 85721, USA
[4] Bard College, 30 Campus Rd, Annandale-On-Hudson, NY 12504, USA
[5] Institute of Astrophysics and Space Sciences, Rua das Estrelas 4150-762 Porto, Portugal
[6] Technical University of Denmark, Department of Chemical and Biochemical Engineering, Søltofts Plads 229, Kgs. Lyngby DK 2800, Denmark
[7] School of Earth and Atmospheric Sciences, Georgia Institute of Technology, Atlanta, GA 30332, USA
Received 2024 January 19; revised 2024 March 22; accepted 2024 April 2; published 2024 May 23

Abstract

JWST has created a new era of terrestrial exoplanet atmospheric characterization, and with it, the possibility to detect potential biosignature gases like CH_4. Our interpretation of exoplanet atmospheric spectra, and the veracity of these interpretations, will be limited by our understanding of atmospheric processes and the accuracy of input modeling data. Molecular cross sections are essential inputs to these models. The photochemistry of temperate planets depends on photolysis reactions whose rates are governed by the dissociation cross sections of key molecules. H_2O is one such molecule; the photolysis of H_2O produces OH, a highly reactive and efficient sink for atmospheric trace gases. We investigate the photochemical effects of improved H_2O cross sections on anoxic terrestrial planets as a function of host star spectral type and CH_4 surface flux. Our results show that updated H_2O cross sections, extended to wavelengths >200 nm, substantially impact the predicted abundances of trace gases destroyed by OH. The differences for anoxic terrestrial planets orbiting Sun-like host stars are greatest, showing changes of up to 3 orders of magnitude in surface CO levels, and over an order of magnitude in surface CH_4 levels. These differences lead to observable changes in simulated planetary spectra, especially important in the context of future direct-imaging missions. In contrast, the atmospheres of planets orbiting M-dwarf stars are substantially less affected. Our results demonstrate a pressing need for refined dissociation cross-section data for H_2O, where uncertainties remain, and other key molecules, especially at mid-UV wavelengths >200 nm.

Unified Astronomy Thesaurus concepts: Planetary atmospheres (1244); Habitable planets (695); Exoplanet atmospheres (487); Exoplanets (498); Water vapor (1791)

1. Introduction

Recent surveys and statistical analyses have revealed that rocky terrestrial planets are common in the galaxy (Dressing & Charbonneau 2015; Bryson et al. 2020; Dattilo et al. 2023). The launch of JWST, upcoming ground-based instruments and facilities, and the recommendations of the 2020 Astronomy & Astrophysics Decadal Survey have invigorated prospects for the detailed atmospheric characterization of rocky planets in the coming years and decades. Rocky exoplanets with secondary atmospheres, including Earth, our only known example of a life-bearing world, are central to the search for life outside our solar system (Kaltenegger 2017; Schwieterman et al. 2018).

Photochemical studies are needed to understand both the spectroscopic observables and the environments from which these observables originate on temperate, Earth-like planets. For these photochemical studies to be robust, photochemical models require a wide range of inputs, including chemical reaction rates, molecular cross sections, stellar spectra, dry and wet deposition rates, and mixing parameterizations. Models that have been calibrated for a narrow set of conditions, most often the modern Earth or solar system worlds, can err in their

predictions when inputs are not sufficiently complete for vastly different boundary conditions. Moreover, models that have not harmonized their photochemical inputs will yield incompatible predictions. From an observational standpoint, interpretations or retrievals using divergent model inputs will produce conflicting results with reported uncertainties that include unacknowledged systematic errors (e.g., Niraula et al. 2022).

Recently, Ranjan et al. (2020) showed that updates to H_2O cross sections can meaningfully impact predictions of trace gas chemistry on anoxic, prebiotic planets. Specifically, past prescriptions for photochemical models have truncated the H_2O photolysis cross sections at ∼200–208 nm, where the H_2O opacity falls below the typical scattering opacity of the atmosphere, while the ground-state quantum limit for the H–OH bond at room temperature is ∼240 nm. Historically, this truncation has occurred since H_2O is only marginally spectrally active in this region, and its opacity is far too weak to be used to detect water. Despite this, the 200–240 nm range is consequential for atmospheric chemistry in thick, anoxic atmospheres because stellar mid-UV (MUV; 200–300 nm) photons can penetrate into the H_2O-rich troposphere, while higher-energy far-UV (FUV; <200 nm) photons are shielded by overlying CO_2 in the H_2O-poor stratosphere. (In O_2-rich atmospheres like that of modern Earth, most of these photons are shielded in the upper atmosphere by overlying O_2 and O_3 and are therefore of much less importance for H_2O photolysis.)

H_2O photolysis, following Equation (1), is a particularly important reaction because it serves as the main source of OH in these anoxic atmospheres (in contrast, in O_2-rich atmospheres, OH is primarily sourced from the reaction $O(^1D) + H_2O \rightarrow 2OH$, where the $O(^1D)$ is derived from the photolysis of tropospheric ozone). Ranjan et al. (2020) used newly measured H_2O cross sections to show that these previously neglected MUV photons liberate OH radicals in the troposphere, which subsequently react with trace gases such as CH_4 and assist in catalyzing the recombination of CO and O_2 back into CO_2 (via the reaction $CO + OH \rightarrow CO_2 + H$). Consequently, these updates to the H_2O cross sections harmonized divergent photochemical predictions for the oxidation states of prebiotic anoxic terrestrial planet atmospheres and yielded insights into the trace gas abundance and delivery of reducing compounds to the surface of such worlds. These types of advances have been highlighted as a priority for decades (Wen et al. 1989), and are essential to the future characterization of temperate terrestrial exoplanets with secondary atmospheres.

$$H_2O + h\nu \rightarrow H + OH. \qquad (1)$$

CH_4 is a key biosignature gas that JWST could plausibly detect in the atmospheres of rocky planets orbiting cool M-dwarf stars (Krissansen-Totton et al. 2018; Thompson et al. 2022). The thermodynamic and kinetic disequilibria between atmospheric CH_4 and other atmospheric constituents underpins its potential value as a biosignature (Sagan et al. 1993; Wogan & Catling 2020; Krissansen-Totton et al. 2022; Thompson et al. 2022). However, in order to accurately interpret retrieved CH_4 abundances, we must understand the relationship between CH_4 surface flux and CH_4 surface mixing ratio. In other words, for a given planet-star-atmosphere configuration, a measured mixing ratio corresponds to a CH_4-production rate, and that production rate offers insights into plausible CH_4 sources. Because we know values for various biogenic and abiogenic CH_4 fluxes on Earth, it is thus possible in principle to assess the likelihood of biogenic production (Thompson et al. 2022). However, determining the required rate of photochemical production (which is equivalent to the rate of photochemical destruction in steady state), requires accurate photochemical inputs. In addition, H_2O inputs will impact not only CH_4, but also other important trace species, including CO and O_2, which may likewise be critical for interpreting potential biosignature gas combinations (Harman et al. 2015; Schwieterman et al. 2019; Ranjan et al. 2023).

It is not our intent here to fully evaluate the plausibility of assessing abiotic versus biotic CH_4 in a habitable exoplanet, but rather to illustrate the large discrepancies that are possible with incomplete fundamental photochemical inputs and how this may affect the interpretation of future exoplanetary observations. The updated H_2O cross sections from Ranjan et al. (2020) improved upon previously nonexistent measurements for H_2O at habitable temperatures in the MUV, but they still serve as a more conservative estimate, leading to smaller H_2O photolysis rates than may be physically realistic. Additionally, these cross sections have yet to be independently confirmed or reproduced by other groups. By evaluating the impacts of the updated H_2O cross sections and demonstrating the sensitivity of the photochemical model to this vital input, we aim to emphasize the importance of using extended UV cross sections in models of anoxic terrestrial planets and highlight the need to take additional measurements of H_2O

cross sections in the MUV. More broadly, we hope to show that predictions of atmospheric photochemistry on temperate terrestrial planets can depend sensitively on the long-wavelength tail of the photodissociation opacities of major species, which are often prematurely truncated or extrapolated ad hoc rather than measured, demonstrating critical urgency for improved laboratory and ab initio investigations of these fundamental photochemical inputs (e.g., Fortney et al. 2016, 2019).

In this paper, we conduct a series of CH_4 flux-abundance sensitivity tests using various H_2O cross-section prescriptions. We examine both the effects of these cross sections on CH_4 and on associated photochemical products CO and O_2. We perform these sensitivity tests for planets orbiting FGKM-type stars to determine how the CH_4 flux trace gas abundance relationship varies with stellar type for anoxic, temperate, Earth-like exoplanet atmospheres. In Section 2, we describe the methods used to conduct these sensitivity tests, and describe the photochemical model and planetary atmosphere scenarios used to test the sensitivity of these inputs under a range of conditions. In Section 3, we report our results, including impacts to trace gas species and simulated emission, reflection, and transmission spectra. We discuss the implications of our results in Section 4 and conclude in Section 5.

2. Methods

2.1. Cross-section Prescriptions

We conduct a H_2O cross-section sensitivity test using three different prescriptions, shown in Figure 1. This includes the *old* cross sections from Kasting & Walker (1981), which were the default in the Atmos photochemical code prior to the updated measurements from Ranjan et al. (2020). The *new* cross sections are the extrapolation prescription from Ranjan et al. (2020). From 215–230 nm, the measured H_2O cross sections from Ranjan et al. (2020) showed a deviation from the expected log-linear decrease with wavelength. This deviation might have come from the data approaching the noise limits of the instrumentation; to reduce the chance that their predicted water absorption was an overestimate, they modified their measured cross sections into two different prescriptions: a cutoff prescription and an extrapolated prescription. The cutoff prescription took the measured cross sections, but truncated them beyond about 216 nm (Ranjan et al. 2020). The extrapolated cross sections replaced the measured cross sections beyond 205 nm with a log-linear extrapolation of the data from 186–205 nm, to account for the noisiness of the data beyond 205 nm; thus, the new cross sections, and their photochemical impact, should be considered conservative estimates (we evaluate the cutoff versus the extrapolated cross-section prescriptions in Appendix C). The "abrv" prescription is an abbreviated version of the new cross sections, terminating at 200 nm; this termination wavelength was the recommendation for H_2O (Sander et al. 2011) prior to Ranjan et al. (2020), though we note that our H_2O cross sections are not identical to those of Sander et al. (2011) at wavelengths <200 nm. Using the new cross sections with a 200 nm cutoff allows us to conduct tests *all else being equal,* while minimizing the total number of possible permutations.

For the purpose of these sensitivity tests, we use the CO_2 cross sections from Kasting & Walker (1981) rather than the more recent cross sections from Lincowski et al. (2018), which
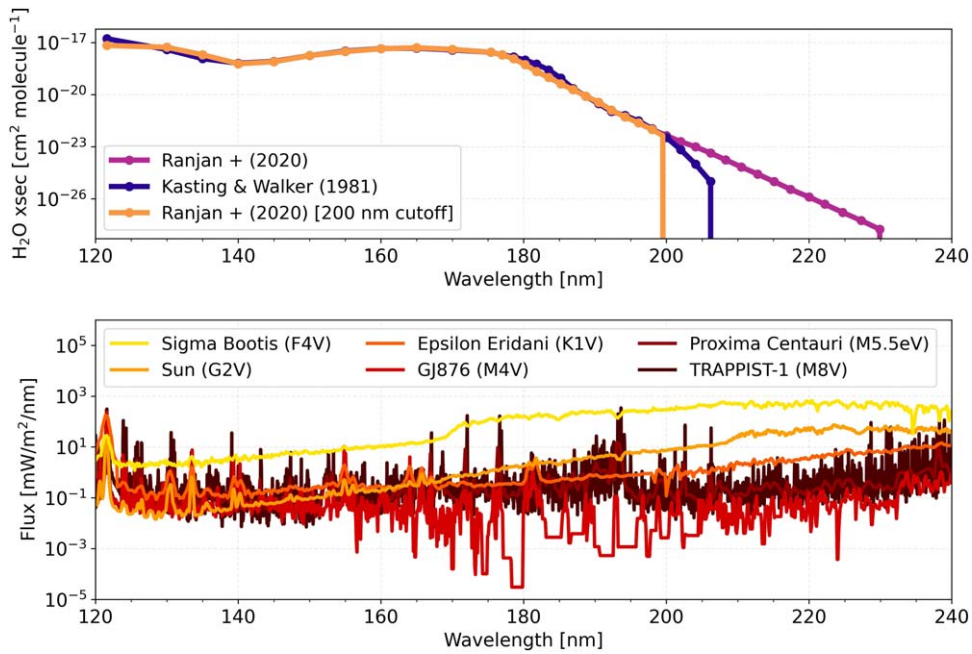
Figure 1. (Top) H$_2$O cross-section prescriptions from 120–240 nm. (Bottom) Spectral energy distribution of the stars modeled in this study, from 120–240 nm.

are extended ad hoc with a log-extrapolation to 225 nm. This choice allows our results to be consistent with the choice of CO$_2$ cross sections from Ranjan et al. (2020). We have, however, examined our results under the assumption of the Lincowski et al. (2018) cross sections and find the major conclusions presented here are unaffected.

2.2. Photochemical Model Description

The photochemical model used in this research is Atmos, a one-dimensional coupled photochemical-climate model (though for the purpose of this research, only the photochemical portion of the model was used). First developed by Kasting et al. (1979), Atmos is frequently updated to keep the chemical reactions rates current (Burkholder et al. 2019), and to improve its capabilities (Zahnle et al. 2006; Arney et al. 2016; Lincowski et al. 2018). Atmos is often used to model terrestrial exoplanet atmospheres (Arney et al. 2016, 2018; Felton et al. 2022; Schwieterman et al. 2022).

Atmos takes in prescribed planetary and stellar parameters, as well as gas species boundary conditions and various fundamental inputs. The atmosphere is divided into 200 equally spaced vertical layers of 0.5 km; flux and mass continuity equations are simultaneously solved at each layer using the reverse Euler method. Once converged, Atmos returns volume mixing ratios for relevant gases at each atmospheric layer.

For the purpose of this research, we used the Archean + haze template described in Arney et al. (2016), with the atmospheric boundary conditions found in Table 2 in Appendix A. We used a modified temperature-pressure profile, setting the surface pressure at 1 bar, and the surface temperature at either 275 or 300 K. The tropospheric water vapor profile is calculated assuming a surface relative humidity of 70% (Manabe & Wetherald 1967). Two surface temperatures were chosen to illustrate the relative impact of the differing H$_2$O cross sections for cool, more water-poor tropospheres versus

warmer, more water-rich tropospheres (within the habitable range). The temperature decreases linearly from the surface to the tropopause (set at 11 km), at which point it becomes an isothermal profile, fixed at 180 K.

2.3. Spectral Model Description

To simulate the spectra of the modeled atmospheres, we use the Spectral Mapping Atmospheric Radiative Transfer code (SMART; Meadows & Crisp 1996; Crisp 1997). SMART takes the temperature-pressure profile and altitude-dependent gas volume mixing ratios from Atmos as input. Contained within SMART is the Line-by-Line Absorption Coefficients (LBLABC) model, which uses spectral line parameters from the HITRAN molecular spectroscopic database (Gordon et al. 2022), but can also incorporate user-supplied data when HITRAN line lists are unavailable. LBLABC calculates the wavelength-dependent opacities from each gas and returns these to SMART. SMART then goes through radiative transfer calculations at each atmospheric layer, incorporating the wavelength-dependent opacities as well as individual gas cross sections and collision-induced absorption coefficients. SMART has been verified for several solar system objects (Tinetti et al. 2006; Robinson et al. 2011; Arney et al. 2014) and is frequently used for simulating exoplanet spectra (Charnay et al. 2015; Lincowski et al. 2018; Lustig-Yaeger et al. 2019; Meadows et al. 2023).

2.4. Stellar Spectra

Photochemical reactions, driven by the actinic flux of the host star, are dependent on the host star's spectrum. To model a broad range of stellar types, we chose six representative stars; three Sun-like (FGK) stars, and three M-type stars. The Sun-like stars include σ Bootis (Segura et al. 2003), an F-type star, the Sun, a G-type star (Thuillier et al. 2004), and ε Eridani (Segura et al. 2003), a K-type star. The three M-type stars include GJ 876 (M4V) (France et al. 2016; Loyd et al. 2016,

Table 1
Stellar Properties

Star	Spectral Type	T_{eff} (K)	Luminosity ($L_\odot$)	Stellar Radius ($R_\odot$)	Distance (pc)
σ Bootis	F4V	6435	3.1541	1.4307	15.8
Sun	G2V	5780	1	1	...
ϵ Eridani	K1V	5039	0.32	0.735	3.2
GJ 876	M4V	3129	0.0122	0.3761	4.69
Proxima Centauri	M5.5 eV	2992	0.001567	0.147	1.3
TRAPPIST-1	M8V	2559	0.000524	0.117	12.1

"v22"; Youngblood et al. 2016), Proxima Centauri (M5.5eV) (Shkolnik & Barman 2014; Loyd et al. 2018; Peacock et al. 2020), and TRAPPIST-1 (M8V) (Peacock et al. 2019a, 2019b). H_2O photolysis is driven by the UV flux of the host star. Table 1 provides the stellar properties of the six host stars modeled here, and Figure 1 shows their UV spectral energy distributions.

2.5. Planetary Scenario

The atmospheres modeled in this work are N_2–CO_2-H_2O atmospheres, consistent with those typically assumed for habitable worlds (e.g., Kopparapu et al. 2013) and within the plausible bounds of the atmospheric composition of the Archean Earth (Arney et al. 2016; Catling & Zahnle 2020). Boundary conditions for each species, including surface flux, volume mixing ratio, and dry deposition rate (if prescribed) are given in Table 2. A key finding from Ranjan et al. (2020) was that their results were sensitive to the assumption of global redox balance. On an anoxic, uninhabited planet, the net delivery of oxidants or reductants to the ocean should be met by a return flux to the atmosphere, assuming no abiotic mechanism to remove excess reduced (or oxidized) materials from the system (e.g., through burial) (Harman et al. 2015; Ranjan et al. 2020). On a planet with life, the production and burial of organic carbon can lead to a net removal of reductants from the ocean-atmosphere system, and the principle of global redox balance does not necessarily apply. Because our focus here is modeling a biotic scenario, we do not enforce global redox balance. We present a second set of simulations assuming abiotic boundary conditions in Appendix B, which also do not enforce global redox balance, in part to be directly comparable with the biotic simulations presented in the main text. However, we tested the sensitivity to imposing global redox for select scenarios and found our results for surface CH_4 mixing ratios to be sensitive to the assumption of global redox balance, similar to the conclusions from Ranjan et al. (2020; see Appendix B for additional details).

Beyond the boundary conditions found in Table 2, we use N_2 as a filler gas, and the total surface pressure is set to 1 bar. We adopt a CO_2 mixing ratio of 2%. Figure 2 shows an example profile plot from our H_2O cross-section sensitivity tests, showing resulting altitude-dependent mixing ratios of key gases using the 275 K new and abbreviated cross sections for the Sun, with the CH_4 flux = 1.1×10^{10} molecules cm^{-2} s^{-1}, which is about one-tenth of Earth's modern CH_4 flux.

To conduct the CH_4 sensitivity tests we vary the CH_4 surface flux, starting at a surface flux of 1.0×10^9 molecules cm^{-2} s^{-1} ($\sim 2.67 \times 10^{-1}$ Tmol yr^{-1}), which is around the upper limit of

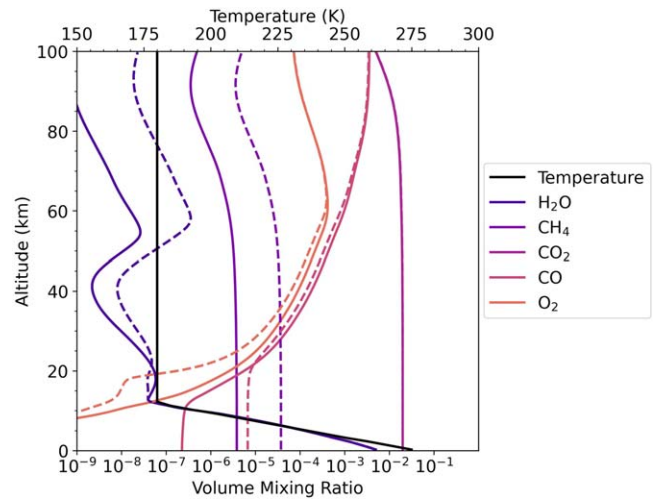**Figure 2.** Example profile plot for an anoxic habitable planet orbiting the Sun, CH_4 = 1.1×10^{10} molecules cm^{-2} s^{-1}. Solid lines show the altitude-dependent volume mixing ratios of key gases modeled using the new H_2O cross sections; dashed lines show the altitude-dependent volume mixing ratios of key gases modeled using the abbreviated H_2O cross sections.

CH_4 flux for serpentinizing systems (Thompson et al. 2022), to a surface flux of 1.0×10^{11} molecules cm^{-2} s^{-1} ($\sim 2.67 \times 10^1$ Tmol yr^{-1}), representing a roughly Earth-like CH_4 flux. (Earth's current methane production levels are around 30 Tmol yr^{-1}, or $\sim 1.12 \times 10^{11}$ molecules cm^{-2} s^{-1} (Thompson et al. 2022)).

3. Results

3.1. H_2O Cross–section Impacts on Trace Gas Relationships

Figure 3 shows the sensitivity of the CH_4 surface volume mixing ratio to CH_4 flux, with the various H_2O cross-section prescriptions and host star stellar types. Figure 4 shows these results for the surface CO volume mixing ratios, and Figure 5 the results for the surface O_2 mixing ratios. Figures 6, 7, and 8 more directly compare the trace gas surface mixing ratios at specific CH_4 fluxes of 10^9, 10^{10}, and 10^{11} molecules cm^{-2} s^{-1}. Generally, the largest differences between atmospheric trace gas volume mixing ratios modeled using the various H_2O cross sections occur in the troposphere, closest to the surface, where the atmosphere is most dense. For this reason, we describe the impacts on the surface volume mixing ratio of CH_4, CO, and O_2. Appendix D describes the impacts to trace gas column densities; notably, Figure 18 shows that CH_4 column density tracks the same relationship as the CH_4 volume mixing ratio, thus conclusions drawn from Figure 3 will hold in either case.

For surface CH_4 volume mixing ratios, the different host star scenarios show differences of up to an order of magnitude, with the largest differences occurring between the new and abbreviated cross sections around a CH_4 flux of 10^{10} molecules cm^{-2} s^{-1}, for the G-type host star. Near the higher CH_4 fluxes, the K- and M-type host stars show surface CH_4 mixing ratios that approach a common value independent of the cross-section prescription. This is consistent with the OH sink becoming saturated. This is true regardless of the cross-section prescription since the MUV flux of these host stars is so low that there are not enough MUV photons available to produce OH through H_2O photolysis and the amount of OH produced is not able to keep up with the increasing amount of CH_4 in the atmosphere. Thus, the OH sink becomes overwhelmed, allowing trace gases
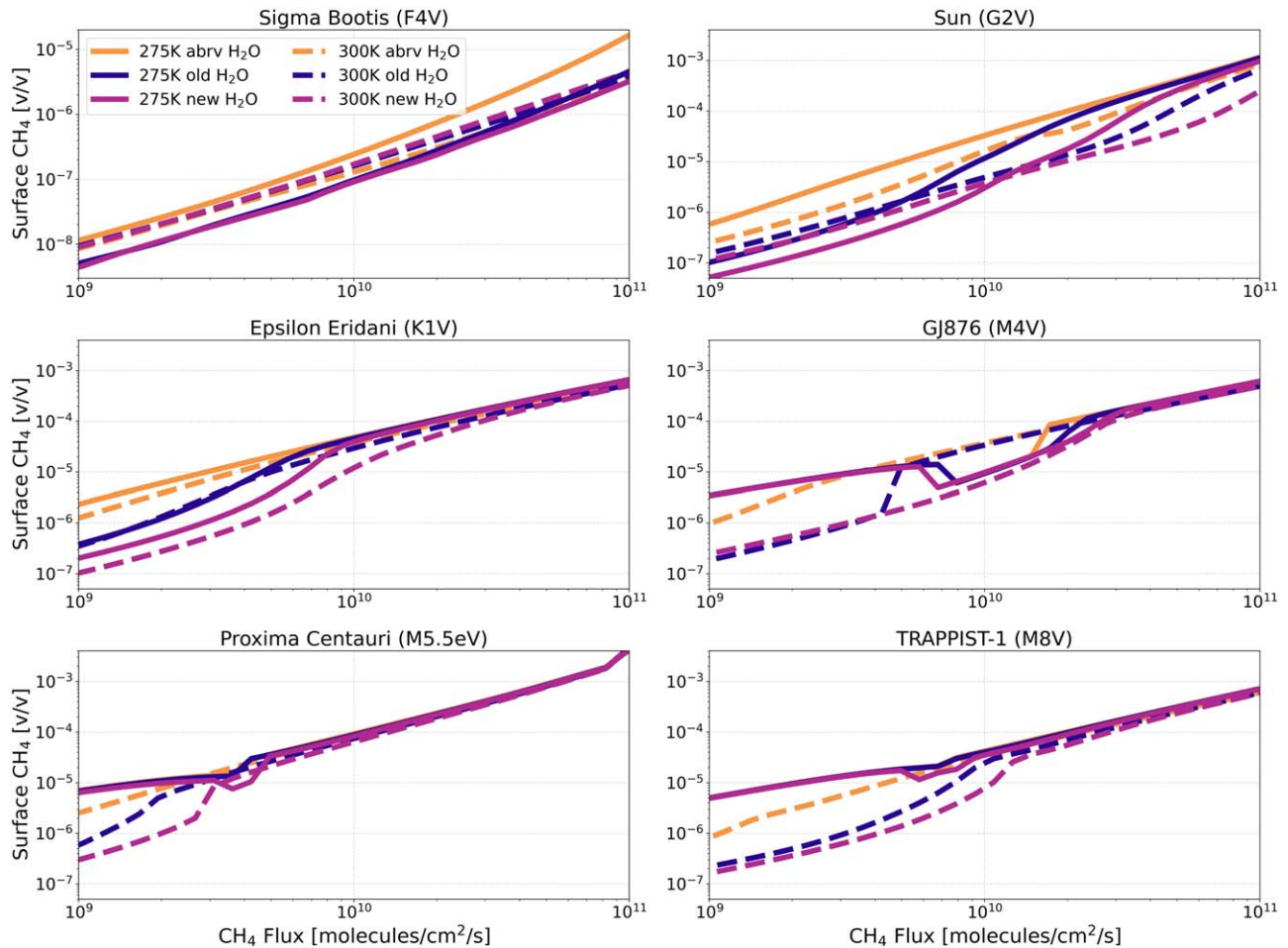
Figure 3. H_2O cross-section sensitivity test; surface CH_4 vs. CH_4 flux for anoxic habitable planets orbiting FGKM-type host stars.

like CH_4 to build up more easily. For the K- and M-type host stars, smaller MUV fluxes lead to the availability of MUV photons being the limiting factor in the production of OH through H_2O photolysis. As more CH_4 is introduced into the atmosphere, OH is more effectively consumed, allowing trace gases to build up that would otherwise be *scrubbed out*. With the greater MUV flux of the G-type host star, OH production reflects the balance between MUV photon availability and H_2O availability; with the drier troposphere of the 275 K regime, we can see the OH sink does not become saturated except at the highest CH_4 fluxes. In the 300 K regime there is more H_2O available for photolysis, with the result that OH production is able to keep up with the increasing CH_4 flux, preventing saturation of the OH sink. In the case of the F-type host star, the MUV flux fuels enough H_2O photolysis that OH production can keep up with the increasing CH_4 flux. We then see much less surface CH_4 buildup (note the more limited scaling of the y-axis for the F-type host star in Figure 3). The difference between the H_2O cross-section cases is more apparent for the drier 275 K temperature regime, and differences increase for larger CH_4 fluxes. Notably, there is some apparent jaggedness to the behavior of the M-type host stars around the middle of the CH_4 flux parameter space for the 275 K temperature regime. This behavior is due to the threshold by which the CH_4 collapses the O_2 levels, and is very sensitive to the choice of input parameters, including the CH_4 flux and cross-section prescription.

Surface CO volume mixing ratios (Figure 4) can show differences of up to 3 orders of magnitude (as in the case of the F-type host star). CO is a photochemical product of CH_4 processing (Schwieterman et al. 2019), so it holds that the maximum differences occur at the lowest CH_4 fluxes. As with surface CH_4, the surface CO mixing ratios for the K- and M-type host stars approach a common value independent of the choice of temperature regime or cross section with increasing CH_4 flux, or in the case of the 275 K regime for the G-type host star. Here, the F-type host star shows the greatest sensitivity to H_2O cross-section prescription.

In Figure 5, we see large variations in the surface O_2, with up to 5 orders of magnitude difference between the abbreviated and new cross sections in the 300 K regime for the F-type host star, and around 3 orders of magnitude difference for the G-type host star. However, it is important to note that these high order of magnitude variations are occurring at very small O_2 mixing ratios, e.g., 7.9×10^{-15} versus 4.9×10^{-10} (as for the F-type host star with a CH_4 flux of 10^9 molecules cm^{-2} s^{-1}, shown in Figure 8). Both these cases are very anoxic, and neither would result in observable spectral features from O_2 or O_3. For the M-type host stars, the surface O_2 volume mixing ratios appear to be more strongly temperature-dependent than the other stellar types, with over 5 orders of magnitude in variation between the 275 and 300 K surface temperatures and associated tropospheric water vapor, but very little change between the old, new, and abbreviated H_2O cross-section
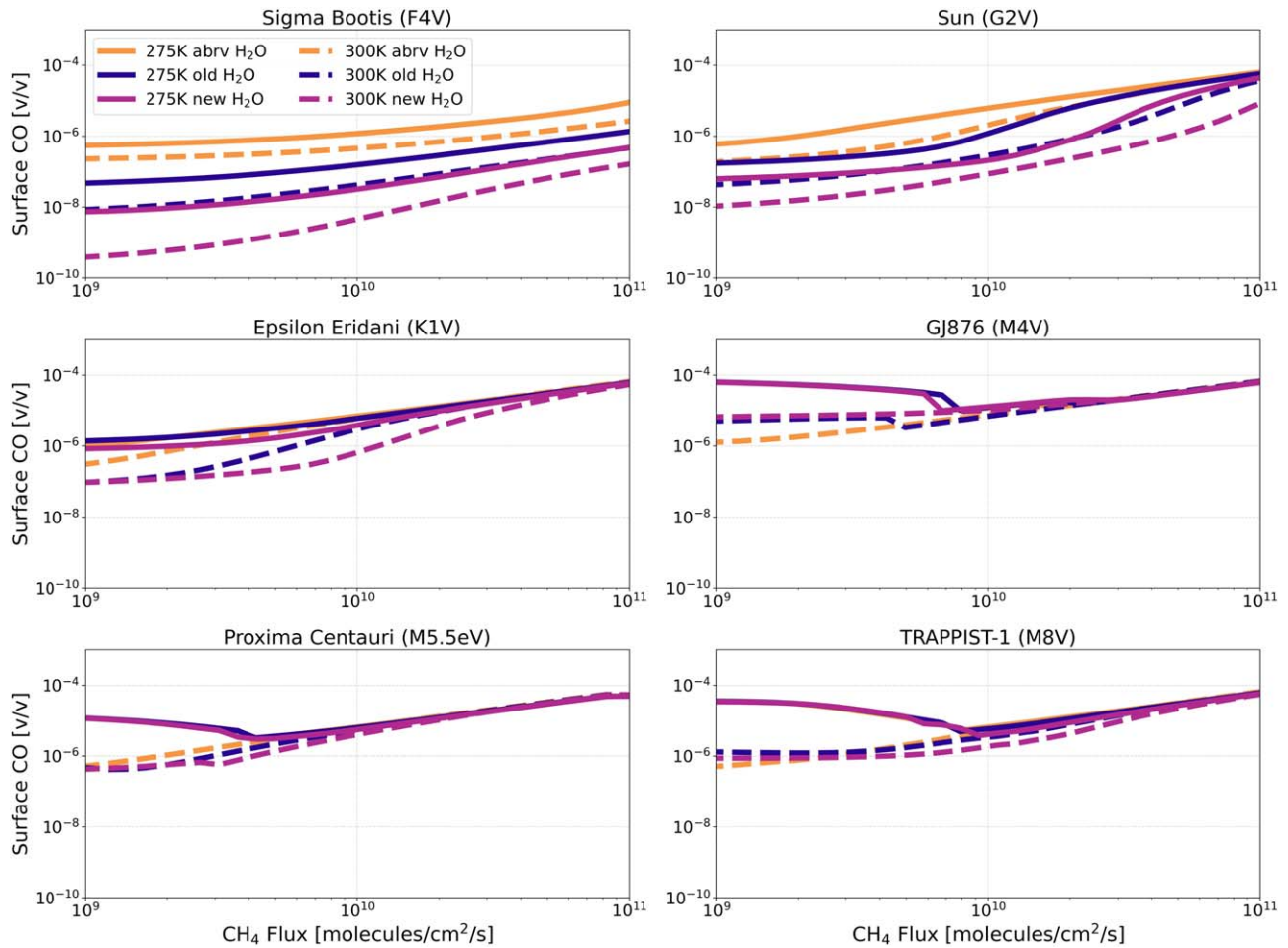
Figure 4. H_2O cross-section sensitivity test; surface CO vs. CH_4 flux for anoxic habitable planets orbiting FGKM-type host stars.

prescriptions. This is primarily attributable to much less H_2O photolysis at the much lower MUV flux of the M-dwarfs relative to the higher-mass stars, which renders changes to the MUV end of the H_2O cross sections less noticeable.

The behavior of the surface O_2 is somewhat different from the other trace gases. Since O_2 is indirectly consumed by CH_4 through oxidation reactions, increasing the CH_4 flux in this scenario leads to decreasing surface O_2. This interaction is clearest with the M-type host stars, where the consumption of O_2 through reactions with CH_4 is strongly temperature dependent. In the 300 K regime, there is enough OH being produced from H_2O photolysis that differences between the cross sections are more apparent. In the 275 K regime, the biggest difference resulting from the various cross-section prescriptions is the flux level where CH_4 starts to lead to a stepwise decrease in O_2; with the new cross sections, the O_2 drops off at slightly smaller CH_4 fluxes, e.g., at 5×10^9 molecules cm^{-2} s^{-1} for the new cross sections, as opposed to 7×10^9 molecules cm^{-2} s^{-1} for the abbreviated cross sections, in the case of TRAPPIST-1 as the host star.

Figure 9 shows relevant chemical reaction rates for the same simulations shown in Figure 2. The difference between the new and abbreviated H_2O photolysis rates is minimal near where CO_2 photolysis is maximal, and greatest where most of the water is present near the surface. The increased H_2O photolysis in the troposphere for the new cross sections corresponds with greater production of OH, which then leads to the greater

consumption of CO, CH_4, CH_3, and other trace gases via their reactions with OH. H_2O photolysis in the upper atmosphere is greater for the abbreviated cross sections than for the new cross sections since as we can see in Figure 2, there is more H_2O in this part of the atmosphere (hence the generally larger OH reaction rates for the abbreviated cross sections in the upper atmosphere). Note that stratospheric CH_4 leads to the production of stratospheric H_2O (Segura et al. 2005).

3.2. Spectral Sensitivity

Depending on the stellar type of the planet's host star, the varying atmospheric trace gas abundances that result from the choice of H_2O cross-section prescription will lead to observable differences in the resulting emission, reflection, and transmission spectra. To show an example of this, we have simulated the emission, reflection, and transmission spectra for a planet orbiting the Sun with a CH_4 flux of 1.1×10^{10} molecules cm^{-2} s^{-1}, equivalent to roughly 3 Tmol $year^{-1}$. This flux is near the maximum possible non-biogenic CH_4 flux given by Krissansen-Totton et al. (2018) and is well within plausible bounds for a methanogenic biosphere. This flux thus lies near a critical threshold for differentiating an abiotic world from an inhabited one. These spectra were generated assuming a cloud coverage of 50% clear sky, 25% cirrus, and 25% alto-stratus.

In the emission spectrum shown in Figure 10, we have labeled features from CO_2 and CH_4. Around 7 μm, we can see that the increased CH_4 resulting from the abbreviated cross sections

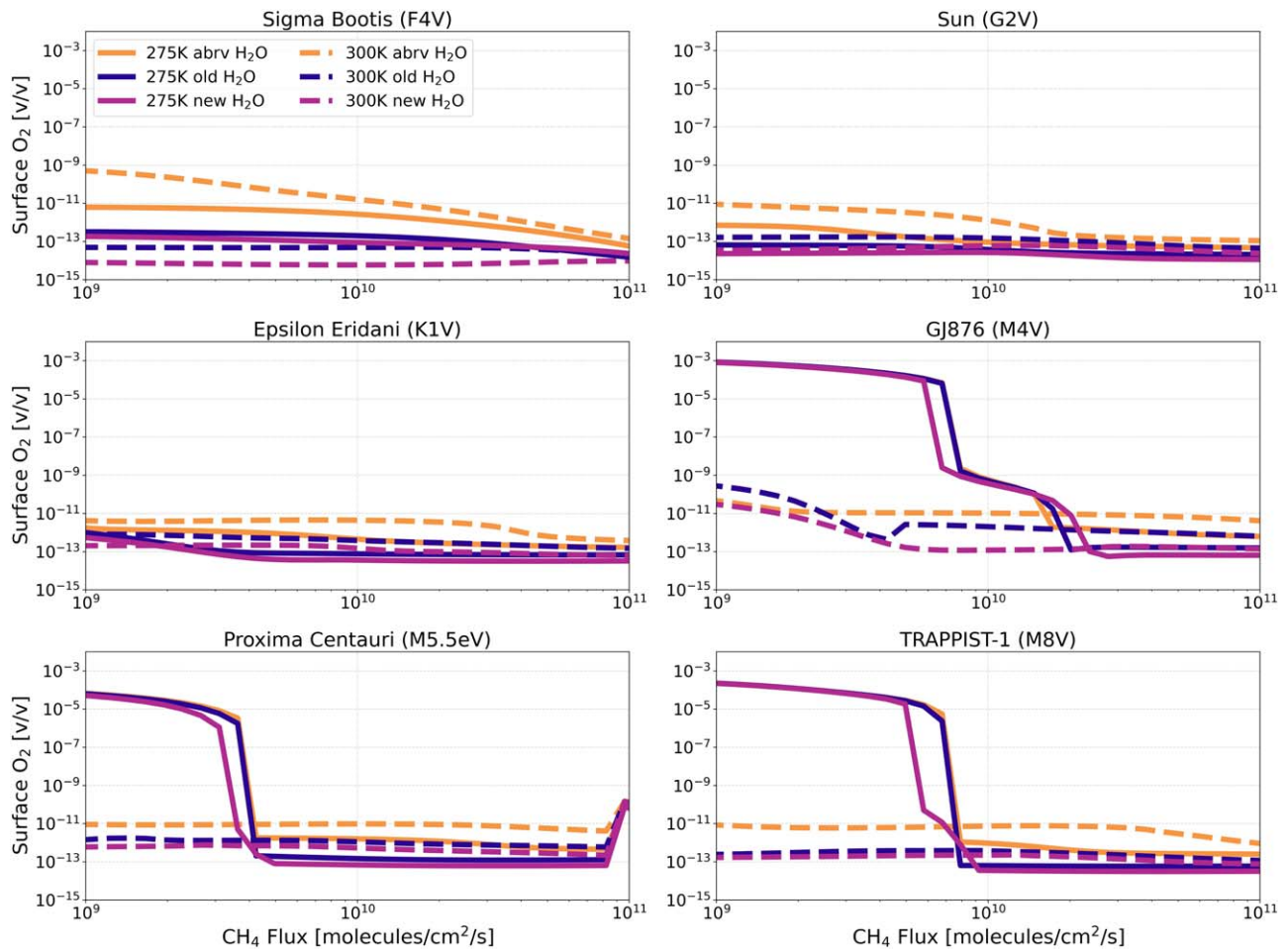**Figure 5.** H$_2$O cross-section sensitivity test; surface O$_2$ vs. CH$_4$ flux for anoxic habitable planets orbiting FGKM-type host stars.
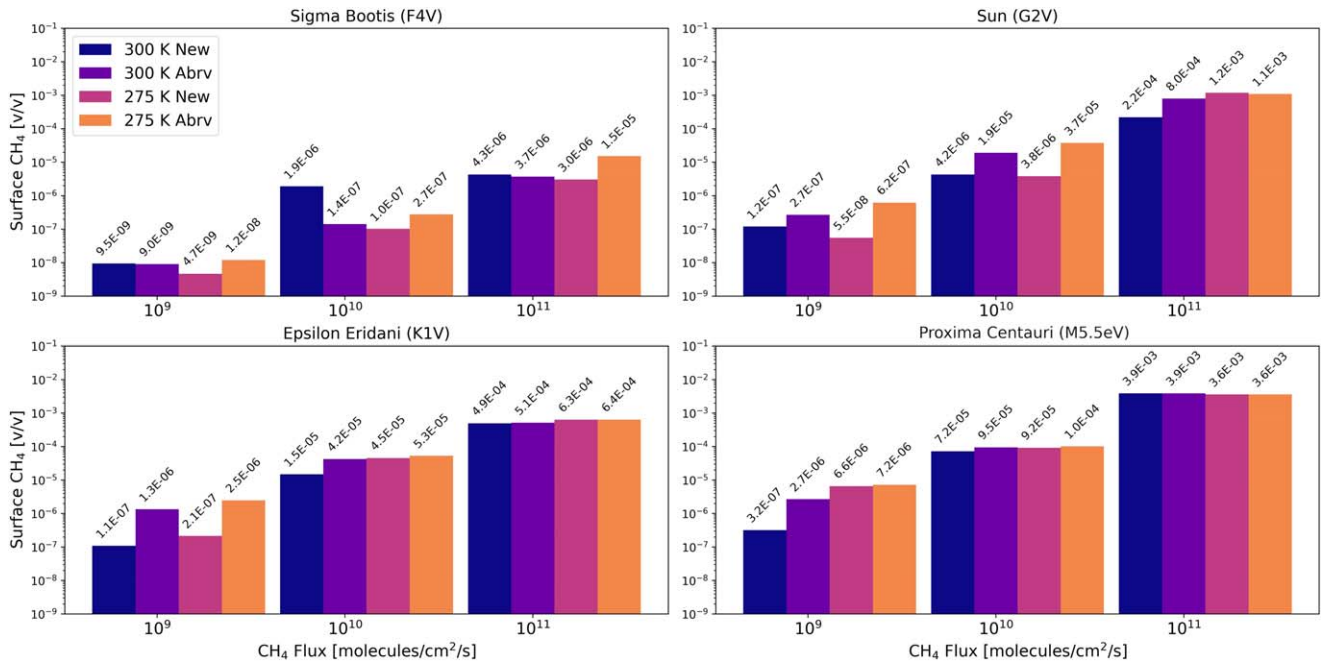

Figure 6. Quantitative difference between CH$_4$ surface mixing ratios for CH$_4$ surfaces fluxes of 10^9, 10^{10}, and 10^{11} molecules cm^{-2} s^{-1}, for anoxic habitable planets modeled using Sigma Bootis, the Sun, Epsilon Eridani, and Proxima Centauri as the host star.
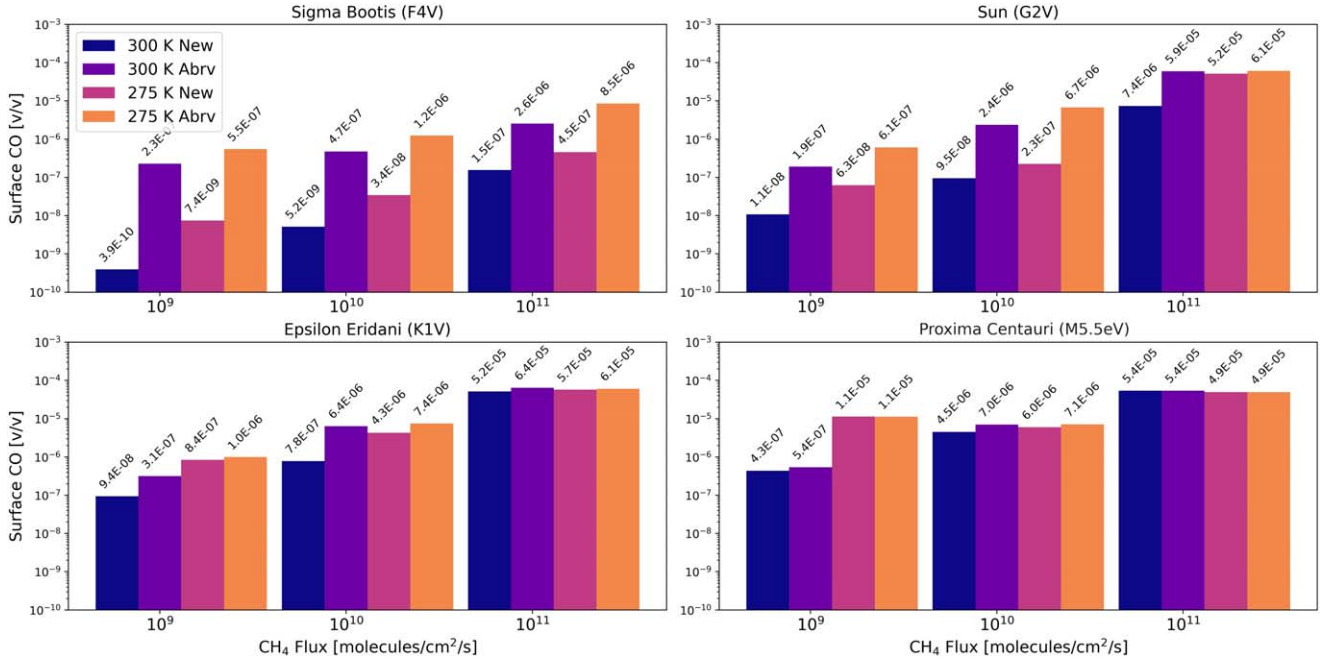
Figure 7. Quantitative difference between CO surface mixing ratios for CH_4 surfaces fluxes of 10^9, 10^{10}, and 10^{11} molecules cm^{-2} s^{-1}, for anoxic habitable planets modeled using Sigma Bootis, the Sun, Epsilon Eridani, and Proxima Centauri as the host star.
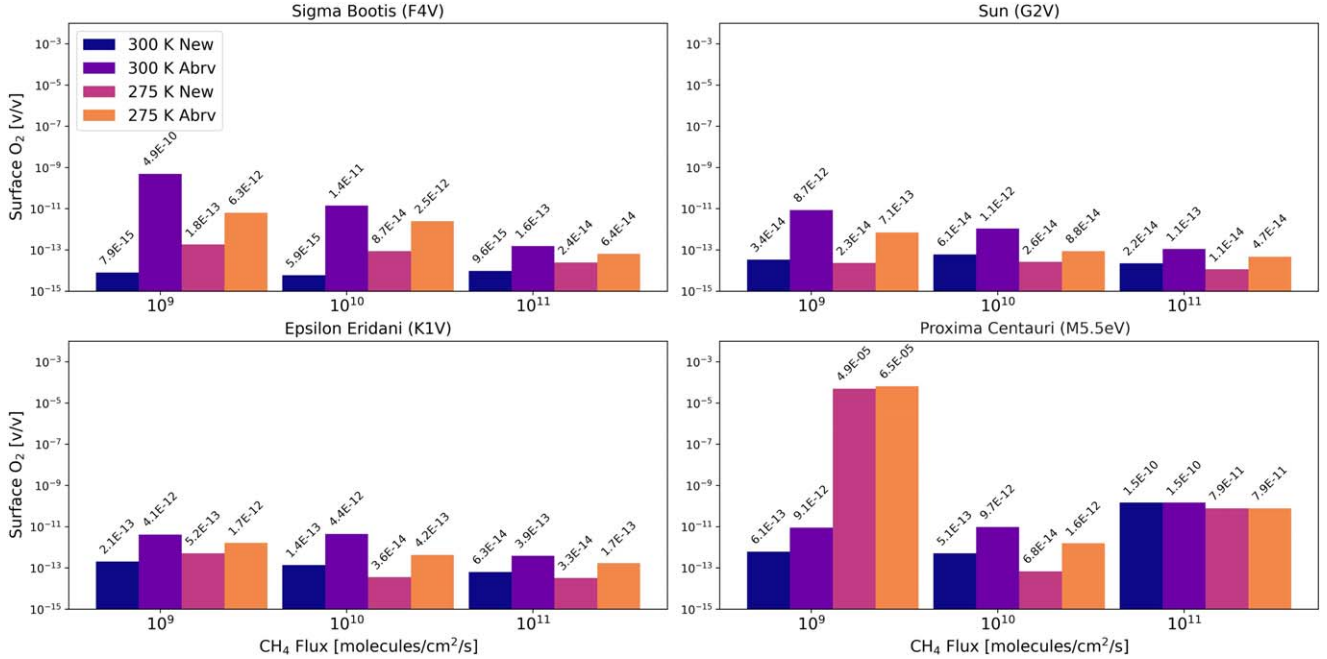

Figure 8. Quantitative difference between O_2 surface mixing ratios for CH_4 surfaces fluxes of 10^9, 10^{10}, and 10^{11} molecules cm^{-2} s^{-1}, for anoxic habitable planets modeled using Sigma Bootis, the Sun, Epsilon Eridani, and Proxima Centauri as the host star.

results in a deeper CH_4 feature. In the reflection and transmission spectra (Figures 11 and 12), we have labeled spectral features from CH_4, CO_2, CO, and H_2O. Most of the deeper features of the abbreviated reflection spectrum are due to greater CH_4, though there is a small contribution from CO at around 2.35 μm. These results are particularly relevant for the upcoming Habitable Worlds Observatory (HWO). In the transmission spectra, most of the features are again due to differences in CH_4 abundance, though there is a very small feature around 4.6 μm due to CO. Although transmission spectra of rocky exoplanets around Sun-like stars are not attainable with JWST, and the proposed HWO will primarily characterize planets in reflected light, it may be possible to characterize some targets through transmission spectroscopy depending on the final HWO design (The LUVOIR Team 2019).

Although we see the largest order of magnitude variations between CH_4 levels for planets orbiting the Sun with a CH_4 flux of 1.1×10^{10} molecules cm^{-2} s^{-1}, the largest absolute differences occur at higher fluxes. These larger absolute differences would not necessarily translate to bigger differences in the observed spectral features because absorption bands can become saturated at higher abundances. Examining the spectral
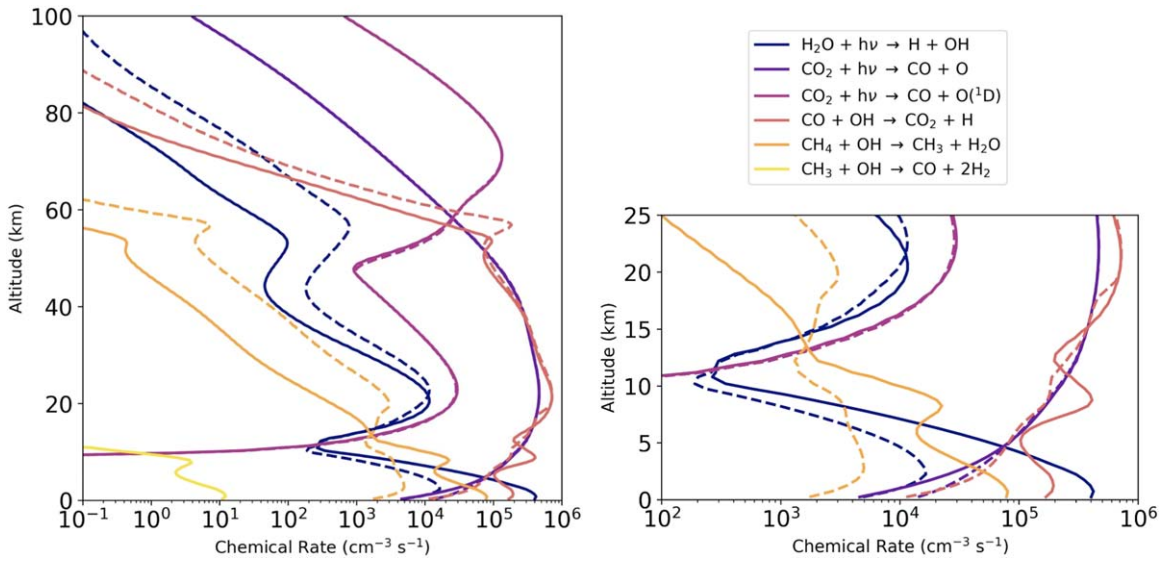
Figure 9. Reaction rates for an anoxic habitable planet orbiting the Sun, $CH_4 = 1.1 \times 10^{10}$ molecules cm^{-2} s^{-1}, for the 275 K temperature regime. Solid lines represent reaction rates modeled using the new H_2O cross sections, dashed lines represent reaction rates modeled using the abbreviated H_2O cross sections. The plot on the left shows the reaction rates up to 100 km; on the right, the rates up to 25 km are shown.
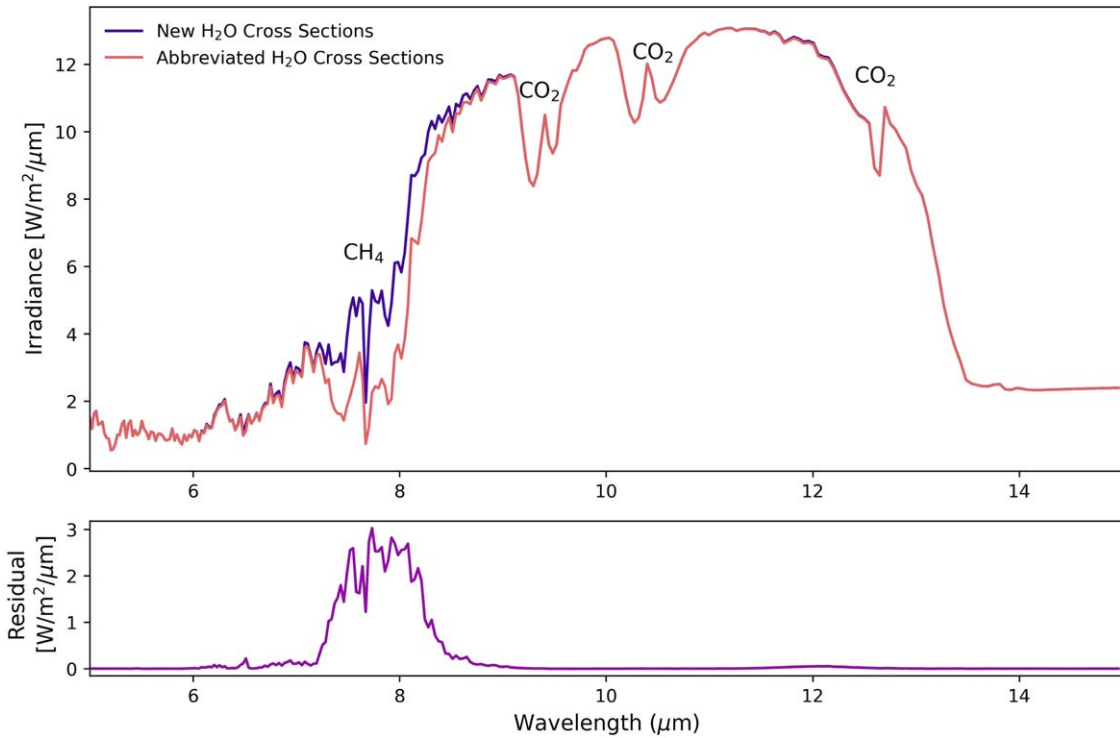

Figure 10. Top: emission spectra comparison between the new and abbreviated cross sections, using the Sun as the host star, where the CH_4 flux $= 1.10 \times 10^{10}$ molecules cm^{-2} s^{-1}. Bottom: plot of the residual, obtained by subtracting the abbreviated H_2O cross-section spectrum from the new H_2O cross-section spectrum.

variation of CH_4 features at each CH_4 flux due to differing H_2O cross sections is beyond the scope of this paper, which is meant to demonstrate that such inputs can have a substantial impact in some regions of flux-abundance space and that they are therefore worth characterizing accurately and precisely.

4. Discussion

The results presented in Section 3 are promising for JWST M-dwarf observation targets, with the M-type host stars showing the least variation with respect to H_2O cross-section prescription. As planets orbiting M-stars are the primary targets of JWST for atmospheric characterization, this means interpreting results from JWST should be less affected by the choice of H_2O cross section in the UV. H_2O cross-section prescription had the greatest impact on the higher-mass host stars; these stars are brighter in the MUV than the lower-mass M-type stars (see Figure 1). FGK-type stars will be the targets of the upcoming HWO, which will be optimized for observing reflected light from small planets in the IR, UV, and optical
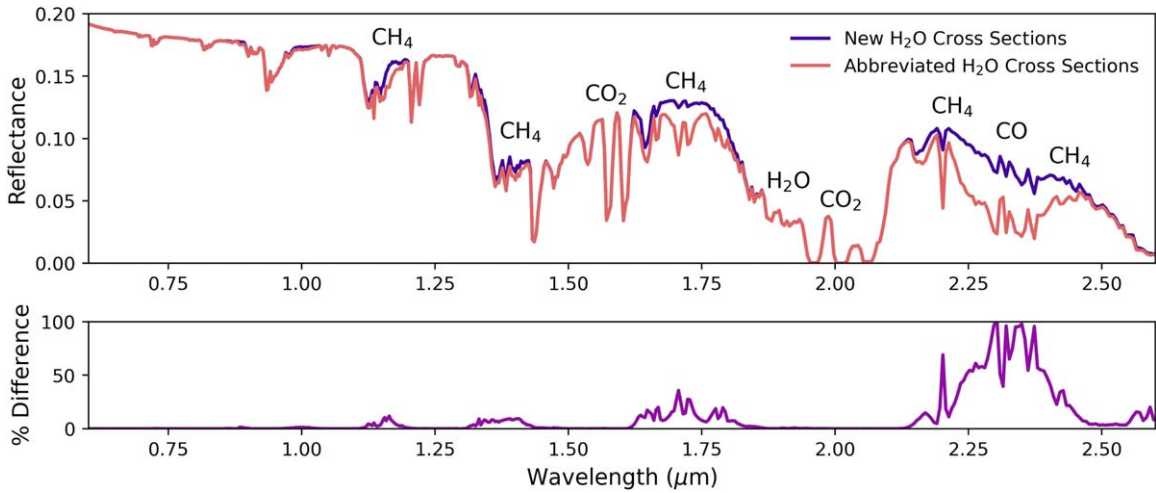
Figure 11. Top: reflection spectra comparison between the new and abbreviated cross sections, using the Sun as the host star, where the CH_4 flux $= 1.10 \times 10^{10}$ molecules cm^{-2} s^{-1}. Bottom: plot of the percent difference between the abbreviated H_2O cross-section spectrum and the new H_2O cross-section spectrum.
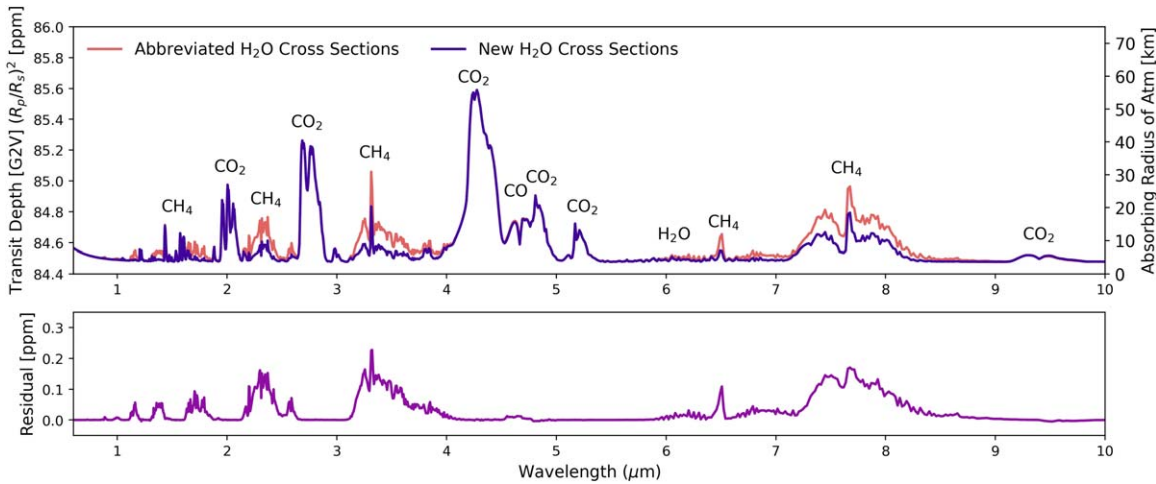

Figure 12. Top: transmission spectra comparison between the new and abbreviated cross sections, using the Sun as the host star, where the CH_4 flux $= 1.10 \times 10^{10}$ molecules cm^{-2} s^{-1}. Bottom: plot of the residual, obtained by subtracting the abbreviated H_2O cross-section spectrum from the new H_2O cross-section spectrum.

(Mamajek & Stapelfeldt 2024). Our results show that for these higher-mass host stars, having accurate H_2O cross sections will be critical for making accurate predictions and correct interpretations of temperate terrestrial exoplanet spectra.

We have tested only an N_2–CO_2–H_2O dominated atmosphere, with a composition similar to that of the Archean Earth. Different atmospheric compositions will be more or less affected by the updated H_2O cross sections; for instance, an oxygen-rich atmosphere with a stratospheric ozone layer that shields water in the troposphere from MUV photons and/or where OH is not primarily sourced from H_2O photolysis (e.g., the modern Earth atmosphere) will not be as sensitive to H_2O cross sections. On the other hand, in our simulations, we keep the surface CO_2 volume mixing ratio fixed at 2%. As demonstrated for Sun-like host stars in Watanabe & Ozaki (2024), higher relative abundances of CO_2 naturally lead to higher rates of CO_2 photolysis and further suppression of H_2O photolysis. The MUV H_2O cross sections would become increasingly important in high-CO_2 cases, owing to the increased CO sourced from CO_2 photolysis combined with a

reduction in OH produced from FUV H_2O photolysis (Akahori et al. 2023).

The updated cross sections are also a conservative estimate, meaning the predicted H_2O photolysis occurring with these cross sections is a lower estimate and actual photolysis rates may be higher (Ranjan et al. 2020). Thus, OH production may be greater in magnitude, and subsequent atmospheric trace gas abundances may be even lower in abundance than what is predicted here (e.g., Appendix C, where we see that using the cutoff prescription from Ranjan et al. 2020 results in around half the amount of surface CO and CH_4 as is generated with the extrapolation prescription). These updated H_2O cross sections differ in the FUV somewhat from previous recommendations (see Figure 1, specifically around 180 nm and 120–140 nm); to have the best cross-section recommendations possible, it is important to further investigate these differences in the FUV range. Further, the MUV cross sections are the result of absorption from (thermally populated) H_2O rotational levels in the first H_2O vibrational level. The cross sections we use for this long-wavelength tail have been measured at one

temperature (292 K), but the temperature-dependent behavior of the cross sections could matter. The effect is likely small at the temperature regimes we have simulated, but discrepancies may result if we wanted to use these MUV cross sections for temperature regimes substantially different from habitable temperatures, especially high temperatures (e.g., steam atmospheres). Ideally, precise temperature-dependent cross sections should be measured (or calculated) and adopted. We have not tested the sensitivity of these updated cross sections to chemical reaction rates; reaction rates previously identified as needing further study (e.g., the reactions identified in Ranjan et al. 2020) may yet lead to further impacts on atmospheric trace gas abundances. Additionally, the CO_2 cross sections used in these simulations also suffer from uncertainty, and it is important to test the sensitivity of the H_2O cross-section prescription to the choice of CO_2 cross-section prescription in order to examine competing effects.

Similar to the conclusions in Watanabe & Ozaki (2024), our results show that CO runaway occurs more easily for planets orbiting the G- and K-type stars at the colder temperature regimes, and does not occur for the F-type star even at the highest CH_4 fluxes. For the M-type host stars at low CH_4 fluxes in the 275 K surface temperature regime, we see moderate CO and O_2 surface mixing ratios (Figure 5). It is important to note that this was only seen in the biotic scenario, where CO is being deposited on the surface at a rate of 1.2×10^{-4} cm s^{-1}, and not in the abiotic scenario (see Appendix B, Figure 15).

We have modeled the impact on three atmospheric gases: CH_4, CO, and trace O_2. These are not the only gases that would be affected by the choice of H_2O cross sections. Any gas that interacts with OH (e.g., phosphine, ethane, methyl chloride, to name a few) will be affected by the increased OH produced by extended H_2O cross sections. Thus, further constraining and testing relationships of other trace gases to these H_2O inputs will be vital for diverse planetary biosignature scenarios (e.g., Domagal-Goldman et al. 2011; Sousa-Silva et al. 2020; Madhusudhan et al. 2021; Huang et al. 2022; Leung et al. 2022). Our results show that the updated H_2O cross sections are essential for the interpretation of future observational data. While the updated cross sections have unprecedented accuracy compared to previous results, additional sensitive experimental results could help distinguish between the conservative extrapolation prescription and the possible higher MUV opacity shown by the measurements. Our results presented in Appendix C show meaningful differences in predicted gas mixing ratios between the extrapolation and *cutoff* H_2O prescriptions presented in Ranjan et al. (2020), which are both conservative prescriptions in terms of their treatment of photodissociation opacity at wavelengths >216 nm. Therefore future, more sensitive measurements of H_2O MUV opacities are justified.

It is also important to consider downstream effects we have not modeled, which may or may not be spectrally observable but will nonetheless have consequences for atmospheric chemistry. For instance, organic haze can start to form at high CH_4/CO_2 ratios (Trainer et al. 2006; Arney et al. 2016, 2018). Given that the updated H_2O cross sections lead to lower CH_4 mixing ratios, a greater CH_4 flux may be required in order to form haze. Further investigation into the effects of these updated cross sections on haze formation is an important topic for future work.

5. Conclusions

Having accurate fundamental inputs, such as photochemical cross sections, is critical for modeling and interpreting the atmospheres of temperate terrestrial exoplanets. Depending on which H_2O cross-section prescription is used, and what wavelength is used as the terminating wavelength, we predict meaningful differences in resulting trace gas abundances. Temperate anoxic planets orbiting higher-mass FGK-type host stars see the largest variations, with trace gas abundances varying by several orders of magnitude depending on the temperature regime, host star, and cross-section prescription. Moreover, these variations can become significant at threshold CH_4 fluxes, which straddle the line between a reasonable abiotic flux and a potentially biotic flux. Depending on the capabilities and noise thresholds of upcoming observatories, these orders of magnitude variations in the CH_4 volume mixing ratios may cause an observable difference in the resulting planetary reflection, emission, and transmission spectra.

The relatively small variations we observe for M-type host stars are a positive result for interpretations of JWST observations of secondary atmospheres—e.g., the H_2O cross-section prescription should not introduce significant uncertainty in interpreting these observations. In contrast, our results indicate that accurate H_2O cross sections will be critical for robust interpretation of observations from HWO, as the chosen prescription can have a significant impact on the modeled atmospheres and simulated spectra for planets orbiting FGK-type stars. Finally, these results also reemphasize the general need to continue investigating fundamental uncertainty in the basic inputs underlying photochemical models, and highlight the critical importance of obtaining empirical cross sections to accurately interpret exoplanet observations.

Appendix A
Biotic Boundary Conditions

Table 2 presents the boundary conditions used for the biotic scenario. Each species boundary condition is specified as a surface flux, a surface mixing ratio, a dry deposition velocity, or as a combination of a surface flux and dry deposition velocity.

Table 2
Atmospheric Species Boundary Conditions

Species	Surface Flux (molecules cm^{-2} s^{-1})	Surface Mixing Ratio (v/v)	Dry Deposition Velocity (cm s^{-1})
O	...	...	1
O_2	...	...	0
H_2O	...	...	0
H	...	...	1
OH	...	...	1
HO_2	...	...	1
H_2O_2	...	...	2×10^{-1}
H_2	1×10^{10}	...	2.4×10^{-4}
CO	1×10^{8}	...	1.2×10^{-4}
HCO	...	...	1
H_2CO	...	...	2×10^{-1}
CH_4	10^{9} - 10^{11}	...	...
CH_3	...	...	1
C_2H_6	...	...	0
NO	...	...	3×10^{-4}
NO_2	...	...	3×10^{-3}
HNO	...	...	1
O_3	...	...	7×10^{-2}
HNO_3	...	...	2×10^{-1}
N	...	...	0
C_3H_2	...	...	0
C_3H_3	...	...	0
CH_3C_2H	...	...	0
CH_2CCH_2	...	...	0
C_3H_5	...	...	0
C_3H_6	...	...	0
C_3H_7	...	...	0
C_3H_8	...	...	0
C_2H_4OH	...	...	0
C_2H_2OH	...	...	0
C_2H_5	...	...	0
C_2H_4	...	...	0
CH	...	...	0
CH_3O_2	...	...	0
CH_3O	...	...	0
CH_2CO	...	...	0
CH_3CO	...	...	0
CH_3CHO	...	...	0
C_2H_2	...	...	0
CH_23	...	...	0
C_2H	...	...	0
C_2	...	...	0
C_2H_3	...	...	0
HCS	...	...	0
CS_2	...	...	0
CS	...	...	0
OCS	...	...	0
S	...	...	0
HS	...	...	0
H_2S	3.5×10^{8}	...	2×10^{-2}
SO_3	...	...	0
HSO	...	...	1
H_2SO_4	...	...	1
SO_2	3×10^{9}	...	1
SO	...	...	0
CO_2	...	2×10^{-2}	...
SO_4 AER	...	...	0.01
S_8 AER	...	...	0.01
HCAER	...	...	0.01
HCAER2	...	...	0.01

Appendix B
Abiotic Scenario

The CH_4 flux sensitivity tests were also conducted for an abiotic scenario; the results of these additional tests are shown in Figures 13–15. The key change from the biotic scenario is the deposition velocity of CO. In the biotic scenario, the deposition velocity of CO is set to 1.2×10^{-4} cm s^{-1}; in the abiotic scenario, this deposition velocity is only 1.0×10^{-8} cm s^{-1}. This decreased CO deposition velocity allows CO to build up more easily in the atmosphere, saturating the OH sink. Because of this, the abiotic results are generally less sensitive to the H_2O cross section. It is plausible that a given planetary scenario could include habitable planets with CO deposition rates between the biotic and abiotic limits we have used in these two scenarios. Thus, these two scenarios serve more generally as upper and lower limits of how the H_2O cross-section prescriptions could impact planetary atmospheres.

For this abiotic scenario, we also conducted a limited sensitivity test to investigate the impact of enforcing a global redox balance. The redox balance hypothesis is often assumed, but is as of yet unproven. To conduct this test, we used the G-type host star with the 275 K surface temperature and a CH_4 surface flux of 1.0×10^{10} molecules cm^{-2} s^{-1}. We adjusted the H_2 surface flux until global redox was attained, which occurred at a H_2 flux of around 4.4×10^{11} molecules cm^{-2} s^{-1}. With global redox imposed, we found the difference between the surface CH_4 volume mixing ratios for the new and abbreviated H_2O cross sections was minimized (though they still differed by about 5%). The resulting surface CO mixing ratios were still larger for the abbreviated cross sections by about an order of magnitude. These results are consistent with the results from Ranjan et al. (2020), who showed that assuming global redox balance decreased the impact of the H_2O cross-section prescription to surface CH_4, but the impact on surface CO remained.
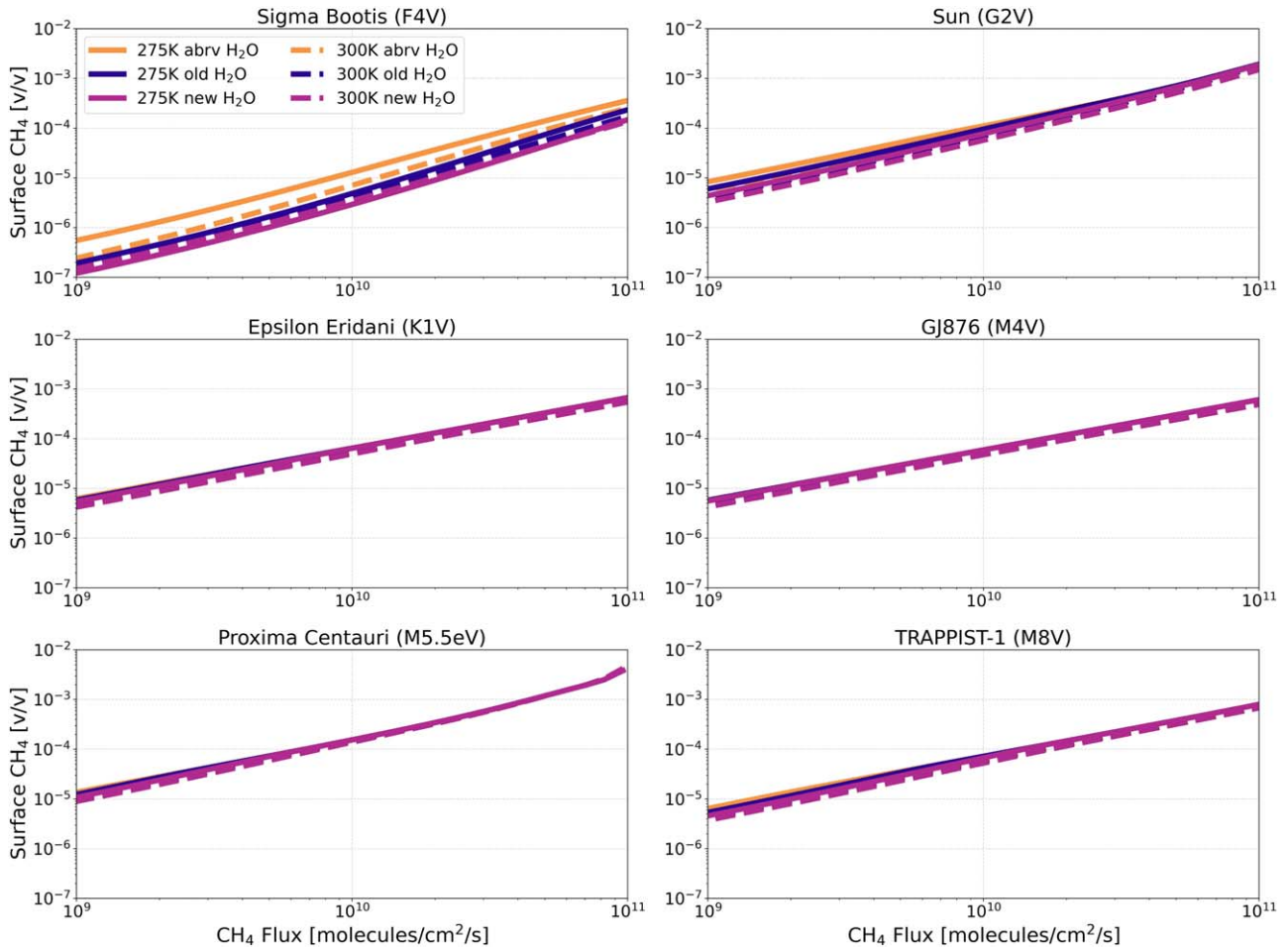

Figure 13. Abiotic H_2O cross-section sensitivity test; surface CH_4 vs. CH_4 flux for planets orbiting FGKM-type host stars.
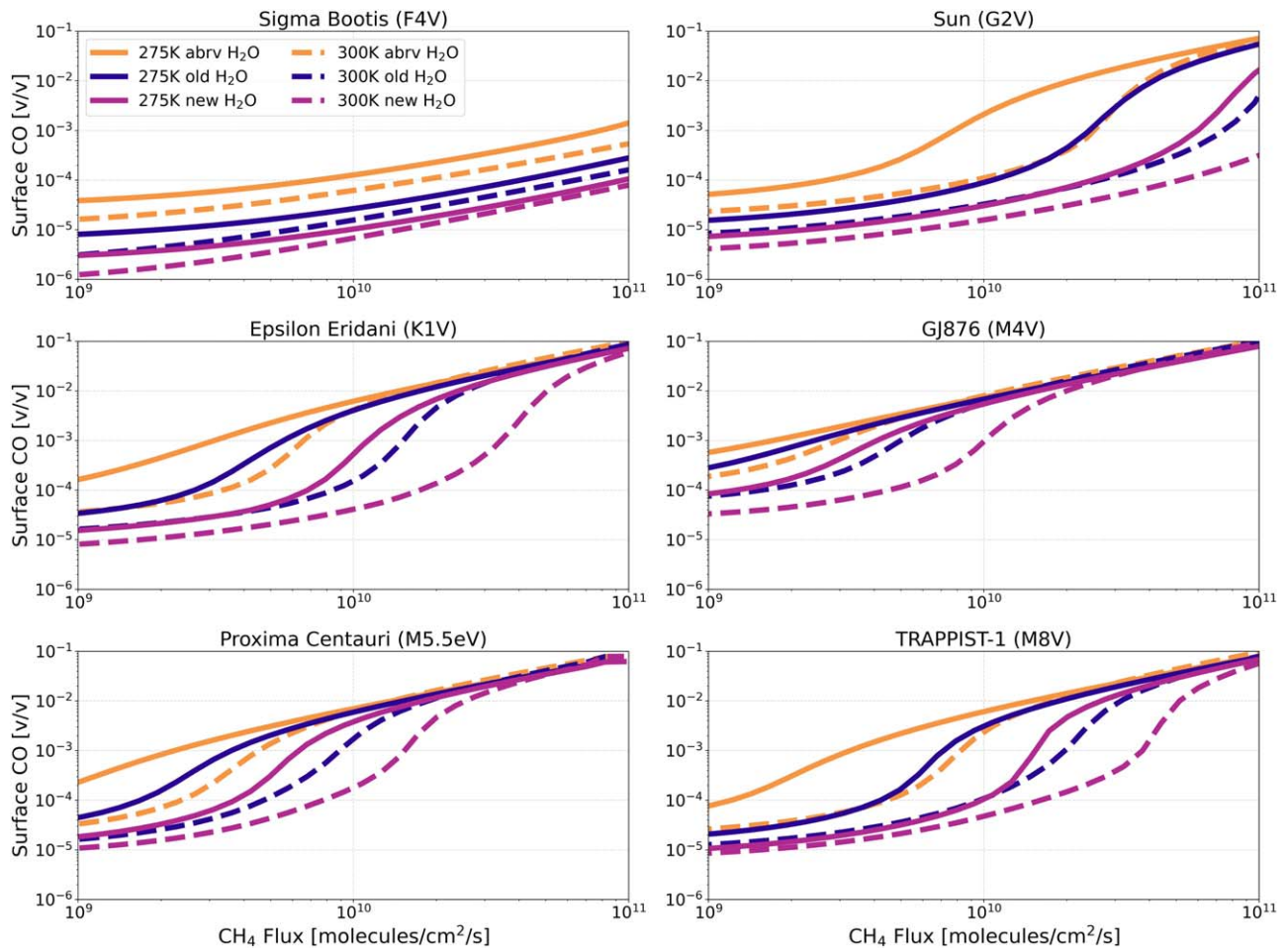
Figure 14. Abiotic H_2O cross-section sensitivity test; surface CO vs. CH_4 flux for planets orbiting FGKM-type host stars.
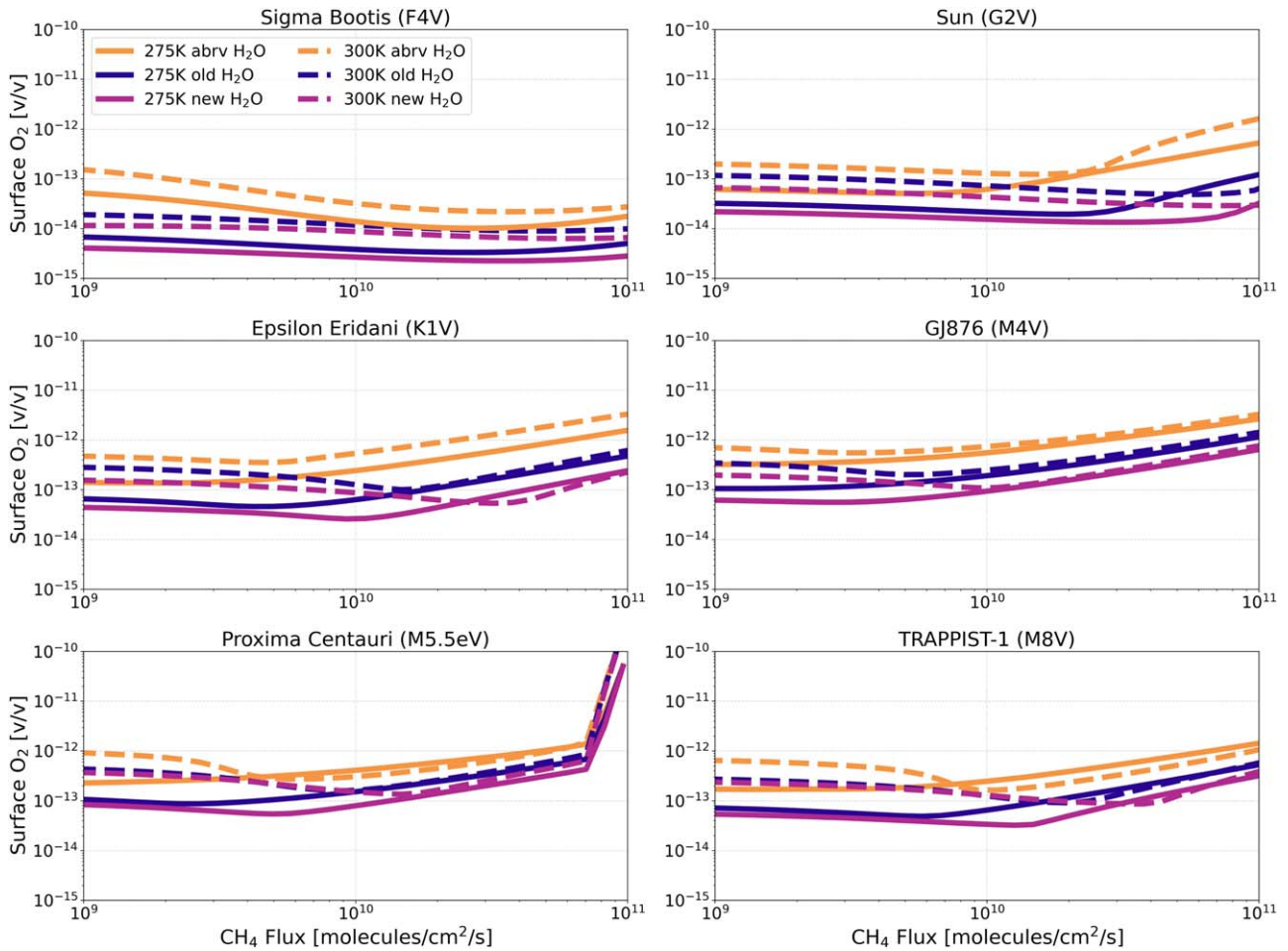
Figure 15. Abiotic H_2O cross-section sensitivity test; surface O_2 vs. CH_4 flux for planets orbiting FGKM-type host stars.

Appendix C
Cutoff versus Extrapolated Cross-section Prescriptions

Figure 16 is a modified version of Figure 1, which shows the H_2O cross sections as a function of wavelength, now including the cutoff prescription from Ranjan et al. (2020), which terminates around 216 nm. Figure 17 shows the results for H_2O cross-section sensitivity tests using the Sun as a host star, for surface CO and CH_4 as a function of CH_4 surface flux, including the cutoff cross-section prescription.

Although the resulting surface CO and CH_4 volume mixing ratios do not differ by orders of magnitude between the cutoff prescription and the extrapolation prescription, there are still noticeable differences. For CO, the greatest fractional differences occur around 3.22×10^{10} and 2.36×10^{10} molecules cm^{-2} s^{-1} for the 275 and 300 K temperature regimes, respectively, where the extrapolated cross sections result in 2.3 and 2.0 times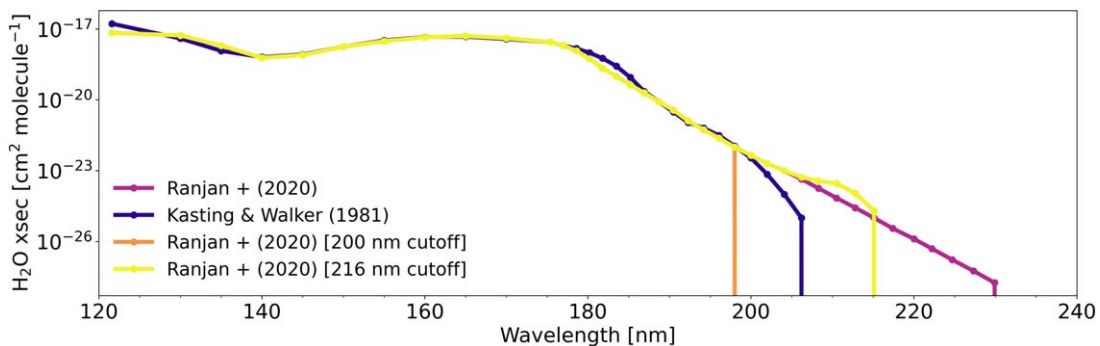 the amount of surface CO as with the cutoff cross sections. For CH_4, the greatest fractional differences occur around 3.22×10^{10} and 9.61×10^{10} molecules cm^{-2} s^{-1} for the 275 and 300 K temperature regimes, respectively, where the extrapolated cross sections result in 1.8 and 1.5 times the amount of surface CH_4 as with the cutoff cross sections.

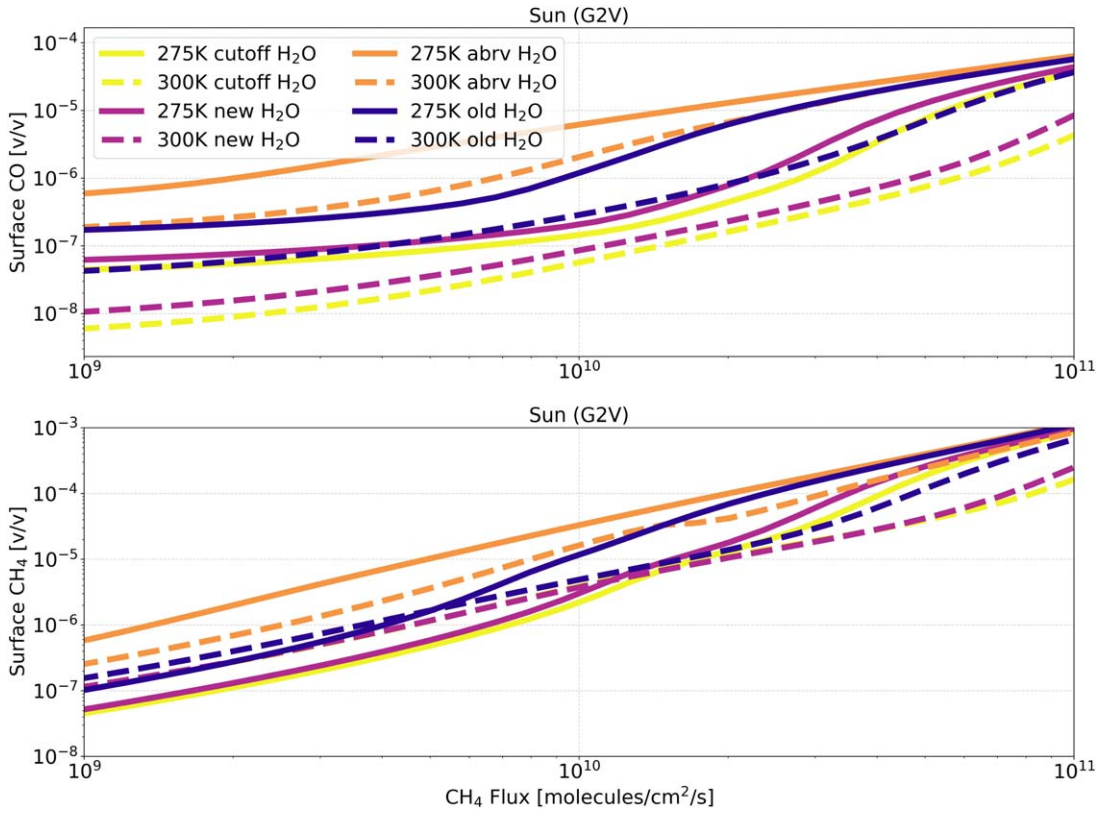**Figure 16.** H_2O cross-section prescriptions from 120–240 nm, including the cutoff prescription.

Figure 17. Biotic H_2O cross-section sensitivity test, including the cutoff prescription, using the Sun as a host star. (Top): surface CO vs. CH_4 flux. (Bottom): surface CH_4 vs. CH_4 flux.

Appendix D
Column Density Relationships

Because the reflected and emitted light spectra of planetary atmospheres are dependent on the column density of a gas, rather than its surface mixing ratio, we reproduce Figures 3–5 by showing the column density as the dependent variable. Importantly, we show that the differences in the CH_4 column densities from H_2O cross-section prescription (Figure 18) closely follow the same relationships shown in Figure 3 for CH_4 surface mixing ratios. This is because, as seen in Figure 2, the CH_4 vertical profiles run parallel, keeping the same difference regardless of the altitude.

On the other hand, CO shows the greatest differences at the surface; above about 20 km, the difference between the vertical profiles goes to zero. Since most of the atmospheric CO is present above 20 km, Figure 19, showing CO column density versus CH_4 flux, exhibits a different relationship from Figure 4.

This is most apparent with the F-type host star, which has a CO column density from $1–4 \times 10^{20}$ molecules cm^{-2} regardless of the surface CH_4 flux or H_2O cross-section prescription. For this host star, the increased CH_4 flux leads to more H_2O production through the reaction of the reaction $OH + CH_4 \rightarrow CH_3 + H_2O$. The CH_3 produced in this reaction can further interact with OH in the reaction $OH + CH_3 \rightarrow CO + 2H_2$. Likewise, the additional H_2O in the upper atmosphere can undergo photolysis, producing more OH, which then consumes the CO. Because these reactions are occurring higher up in the atmosphere, differences between H_2O cross-section prescriptions in the MUV have less of an impact.

For the O_2 column density shown in Figure 20, we do see a similar relationship as in Figure 5, though to a smaller degree. This is because, as with CO, most of the O_2 is present at more significant levels above about 20 km, and smaller changes at the surface become less apparent.
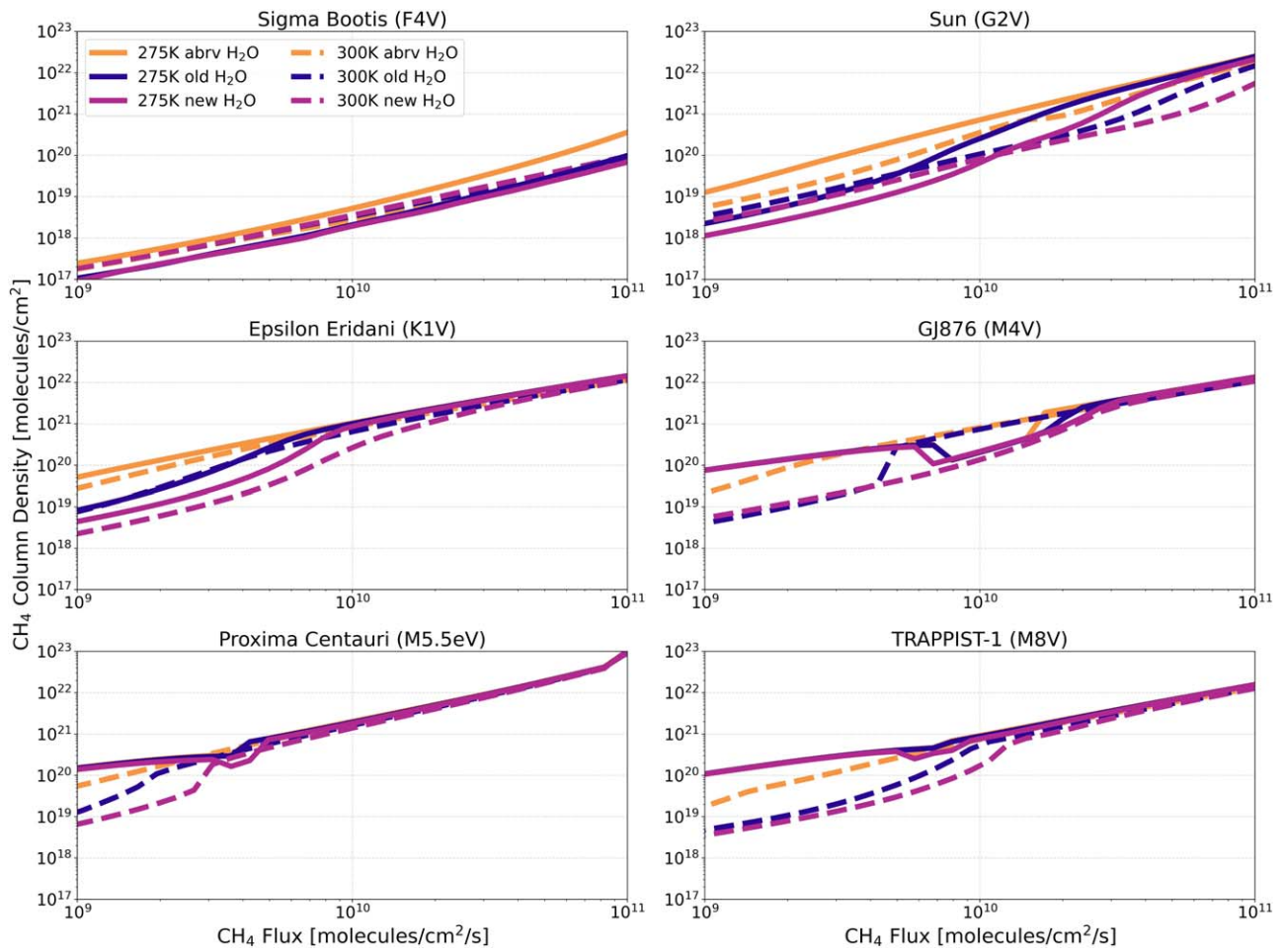
Figure 18. Biotic H_2O cross-section sensitivity test; CH_4 column density vs. CH_4 flux for anoxic habitable planets orbiting FGKM-type host stars.
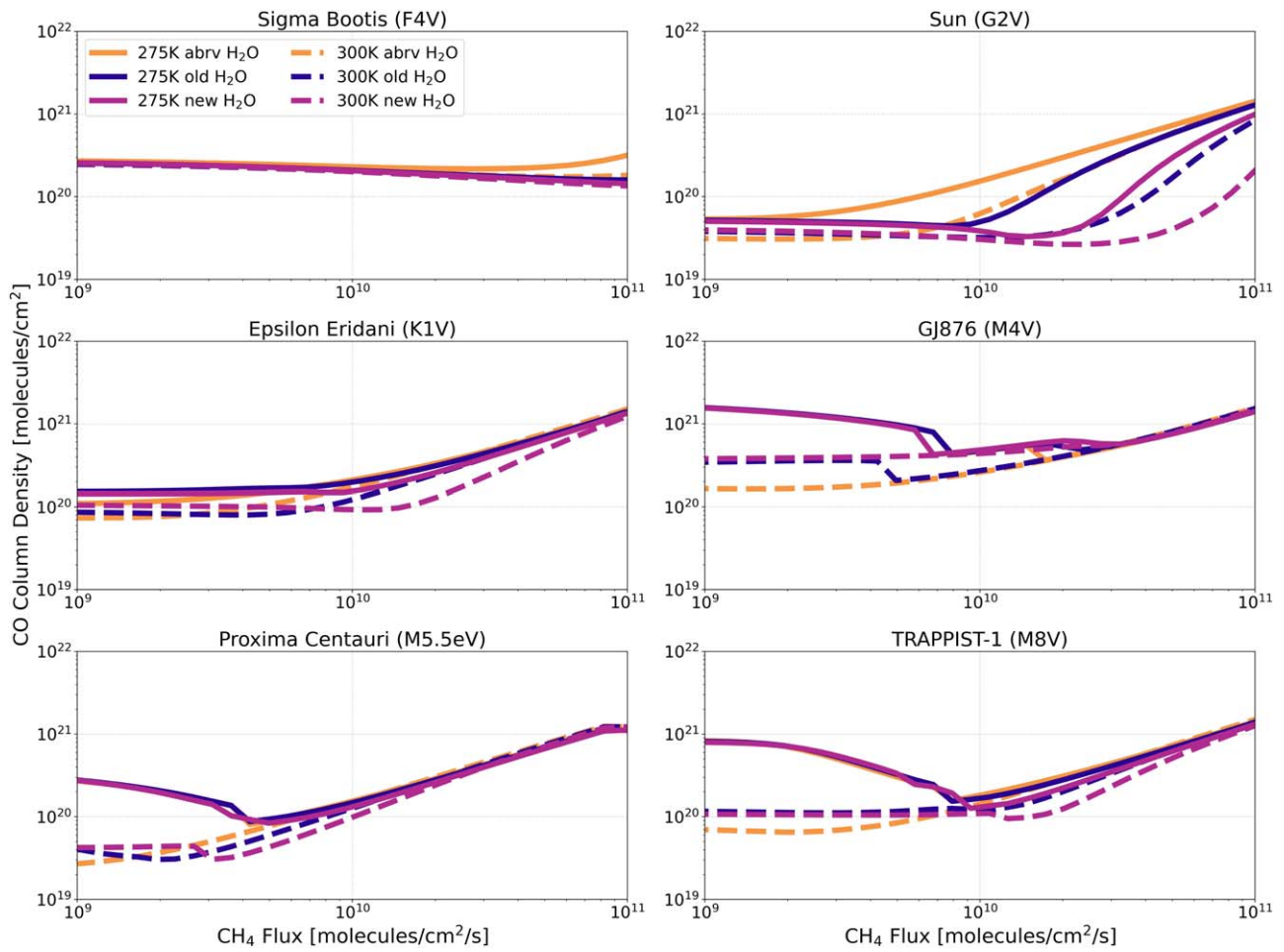
Figure 19. Biotic H_2O cross-section sensitivity test; CO column density vs. CH_4 flux for anoxic habitable planets orbiting FGKM-type host stars.
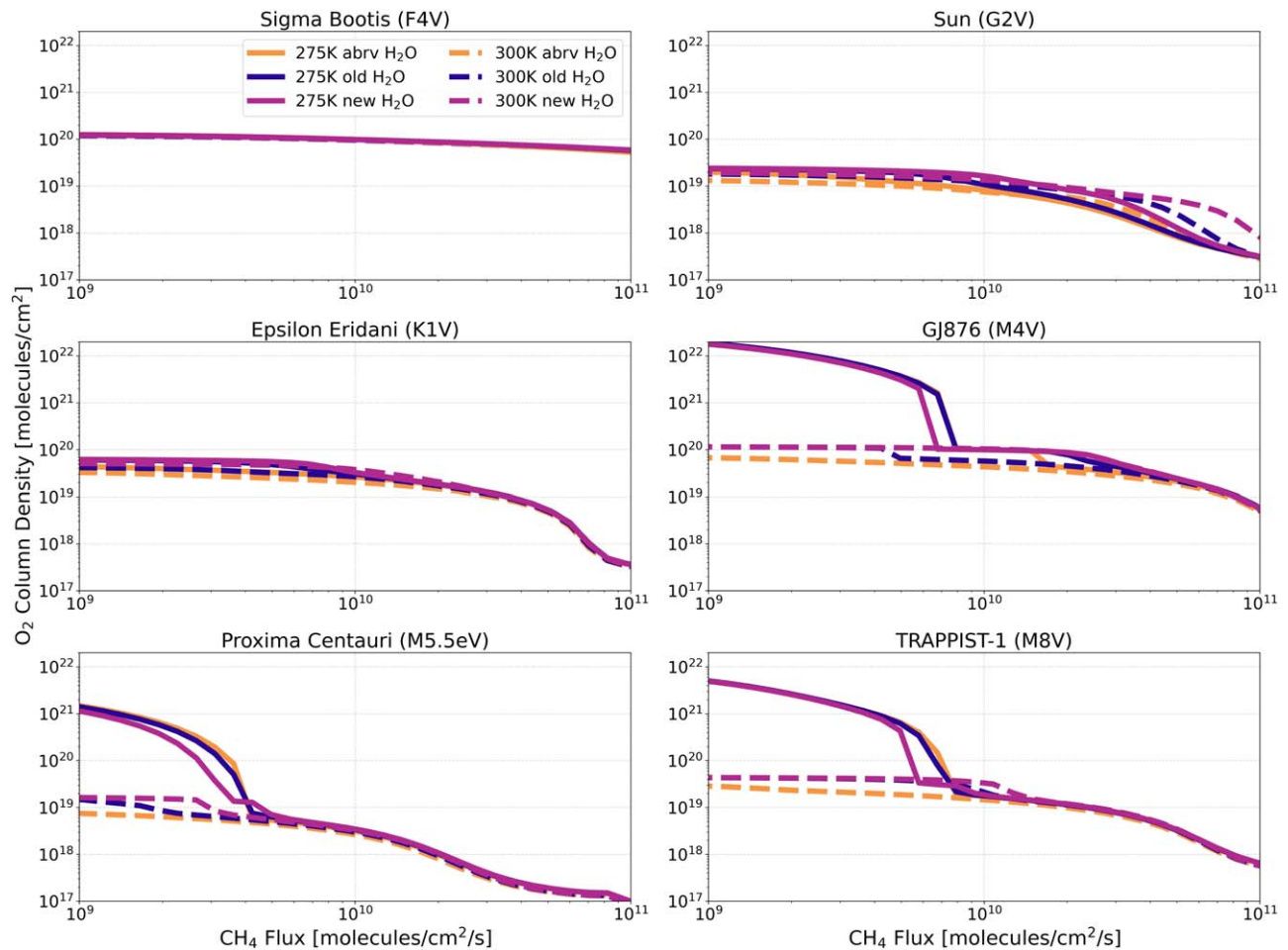
Figure 20. Biotic H_2O cross-section sensitivity test; O_2 column density vs. CH_4 flux for anoxic habitable planets orbiting FGKM-type host stars.

ORCID iDs

Wynter Broussard https://orcid.org/0009-0006-2304-3419
Edward W. Schwieterman https://orcid.org/0000-0002-2949-2163
Sukrit Ranjan https://orcid.org/0000-0002-5147-9053
Clara Sousa-Silva https://orcid.org/0000-0002-7853-6871
Alexander Fateev https://orcid.org/0000-0003-2863-2707

References

Akahori, A., Watanabe, Y., & Tajika, E. 2023, arXiv:2311.06882
Arney, G., Domagal-Goldman, S. D., Meadows, V. S., et al. 2016, AsBio, 16, 873
Arney, G., Domagal-Goldman, S. D., & Meadows, V. S. 2018, AsBio, 18, 311
Arney, G., Meadows, V., Crisp, D., et al. 2014, JGRE, 119, 1860
Bryson, S., Coughlin, J., Batalha, N. M., et al. 2020, AJ, 159, 279
Burkholder, J. B., Sander, S. P., Abbatt, J., et al. 2019, Chemical Kinetics and Photochemical Data for Use in Atmospheric Studies Evaluation No. 19, NASA JPL, https://jpldataeval.jpl.nasa.gov/
Catling, D. C., & Zahnle, K. J. 2020, SciA, 6, eaax1420
Charnay, B., Meadows, V., Misra, A., Leconte, J., & Arney, G. 2015, ApJL, 813, L1
Crisp, D. 1997, GeoRL, 24, 571
Dattilo, A., Batalha, N. M., & Bryson, S. 2023, AJ, 166, 122
Domagal-Goldman, S. D., Meadows, V. S., Claire, M. W., & Kasting, J. F. 2011, AsBio, 11, 419
Dressing, C. D., & Charbonneau, D. 2015, ApJ, 807, 45
Felton, R. C., Bastelberger, S. T., Mandt, K. E., et al. 2022, JGRE, 127, e06853
Fortney, J. J., Robinson, T. D., Domagal-Goldman, S., et al. 2016, arXiv:1602.06305

Fortney, J. J., Robinson, T. D., Domagal-Goldman, S., et al. 2019, Astro2020: Decadal Survey on Astronomy and Astrophysics, Science White Papers, 146
France, K., Loyd, R. O. P., Youngblood, A., et al. 2016, ApJ, 820, 89
Gordon, I. E., Rothman, L. S., Hargreaves, R. J., et al. 2022, JQSRT, 277, 107949
Harman, C. E., Schwieterman, E. W., Schottelkotte, J. C., & Kasting, J. F. 2015, ApJ, 812, 137
Huang, J., Seager, S., Petkowski, J. J., Ranjan, S., & Zhan, Z. 2022, AsBio, 22, 171
Kaltenegger, L. 2017, ARA&A, 55, 433
Kasting, J. F., Liu, S. C., & Donahue, T. M. 1979, JGR, 84, 3097
Kasting, J. F., & Walker, J. C. G. 1981, JGR, 86, 1147
Kopparapu, R. K., Ramirez, R., Kasting, J. F., et al. 2013, ApJ, 765, 131
Krissansen-Totton, J., Garland, R., Irwin, P., & Catling, D. C. 2018, AJ, 156, 114
Krissansen-Totton, J., Thompson, M., Galloway, M. L., & Fortney, J. J. 2022, NatAs, 6, 189
Leung, M., Schwieterman, E. W., Parenteau, M. N., & Fauchez, T. J. 2022, ApJ, 938, 6
Lincowski, A. P., Meadows, V. S., Crisp, D., et al. 2018, ApJ, 867, 76
Loyd, R. O. P., France, K., Youngblood, A., et al. 2016, ApJ, 824, 102
Loyd, R. O. P., Shkolnik, E. L., Schneider, A. C., et al. 2018, ApJ, 867, 70
Lustig-Yaeger, J., Meadows, V. S., & Lincowski, A. P. 2019, AJ, 158, 27
Madhusudhan, N., Piette, A. A. A., & Constantinou, S. 2021, ApJ, 918, 1
Mamajek, E., & Stapelfeldt, K. 2024, arXiv:2402.12414
Manabe, S., & Wetherald, R. T. 1967, JAS, 24, 241
Meadows, V. S., & Crisp, D. 1996, JGR, 101, 4595
Meadows, V. S., Lincowski, A. P., & Lustig-Yaeger, J. 2023, PSJ, 4, 192
Niraula, P., de Wit, J., Gordon, I. E., et al. 2022, NatAs, 6, 1287
Peacock, S., Barman, T., Shkolnik, E. L., Hauschildt, P. H., & Baron, E. 2019a, ApJ, 871, 235
Peacock, S., Barman, T., Shkolnik, E. L., et al. 2019b, ApJ, 886, 77

Peacock, S., Barman, T., Shkolnik, E. L., et al. 2020, ApJ, 895, 5

Ranjan, S., Schwieterman, E. W., Harman, C., et al. 2020, ApJ, 896, 148

Ranjan, S., Schwieterman, E. W., Leung, M., Harman, C. E., & Hu, R. 2023, ApJL, 958, L15

Robinson, T. D., Meadows, V. S., Crisp, D., et al. 2011, AsBio, 11, 393

Sagan, C., Thompson, W. R., Carlson, R., Gurnett, D., & Hord, C. 1993, Natur, 365, 715

Sander, S. P., Abbatt, J., Barker, J. R., et al. 2011, Chemical Kinetics and Photochemical Data for Use in Atmospheric Studies Evaluation Number 17, NASA JPL, https://jpldataeval.jpl.nasa.gov/

Schwieterman, E. W., Kiang, N. Y., Parenteau, M. N., et al. 2018, AsBio, 18, 663

Schwieterman, E. W., Olson, S. L., Pidhorodetska, D., et al. 2022, ApJ, 937, 109

Schwieterman, E. W., Reinhard, C. T., Olson, S. L., et al. 2019, ApJ, 874, 9

Segura, A., Krelove, K., Kasting, J. F., et al. 2003, AsBio, 3, 689

Segura, A. A., Kasting, J. F., Meadows, V., et al. 2005, AsBio, 5, 706

Shkolnik, E. L., & Barman, T. S. 2014, AJ, 148, 64

Sousa-Silva, C., Seager, S., Ranjan, S., et al. 2020, AsBio, 20, 235

The LUVOIR Team 2019, arXiv:1912.06219

Thompson, M. A., Krissansen-Totton, J., Wogan, N., Telus, M., & Fortney, J. J. 2022, PNAS, 119, e2117933119

Thuillier, G., Floyd, L., Woods, T. N., et al. 2004, in Solar Irradiance Reference Spectra, ed. J. M. Pap (Washington, DC: AGU), 171

Tinetti, G., Meadows, V. S., Crisp, D., et al. 2006, AsBio, 6, 34

Trainer, M. G., Pavlov, A. A., DeWitt, H. L., et al. 2006, PNAS, 103, 18035

Watanabe, Y., & Ozaki, K. 2024, ApJ, 961, 1

Wen, J.-S., Pinto, J. P., & Yung, Y. L. 1989, JGR, 94, 957

Wogan, N. F., & Catling, D. C. 2020, ApJ, 892, 127

Youngblood, A., France, K., Loyd, R. O. P., et al. 2016, ApJ, 824, 101

Zahnle, K., Claire, M., & Catling, D. 2006, Geobiology, 4, 271